HHS Public Access

Author manuscript

Cell Rep. Author manuscript; available in PMC 2019 February 07.

Published in final edited form as:

Cell Rep. 2019 January 15; 26(3): 608–623.e6. doi:10.1016/j.celrep.2018.12.090.

Modeling Tumor Phenotypes *In Vitro* with Three-Dimensional Bioprinting

Ellen M. Langer[#1], **Brittany L. Allen-Petersen**[#1], **Shelby M. King**[2], **Nicholas D. Kendsersky**[1], **Megan A. Turnidge**[1], **Genevra M. Kuziel**[1], **Rachelle Riggers**[3], **Ravi Samatham**[3], **Taylor S. Amery**[1], **Steven L. Jacques**[3], **Brett C. Sheppard**[4,5], **James E. Korkola**[3,5], **John L. Muschler**[3,5], **Guillaume Thibault**[3], **Young Hwan Chang**[3], **Joe W. Gray**[3,5,6], **Sharon C. Presnell**[2], **Deborah G. Nguyen**[2], and **Rosalie C. Sears**[1,5,8,*]

[1]Department of Medical and Molecular Genetics, Oregon Health & Science University, Portland, OR 97201, USA

[2]Tissue Applications, Organovo, Inc., San Diego, CA 92121, USA

[3]Department of Biomedical Engineering, Oregon Health & Science University, Portland, OR 97239, USA

[4]Department of Surgery, Oregon Health & Science University, Portland, OR 97239, USA

[5]Knight Cancer Institute, Oregon Health & Science University, Portland, OR 97201, USA

[6]OHSU Center for Spatial Systems Biomedicine, Oregon Health & Science University, Portland, OR 97201, USA

[8]Lead Contact

[#] These authors contributed equally to this work.

SUMMARY

The tumor microenvironment plays a critical role in tumor growth, progression, and therapeutic resistance, but interrogating the role of specific tumor-stromal interactions on tumorigenic phenotypes is challenging within *in vivo* tissues. Here, we tested whether three-dimensional (3D) bioprinting could improve *in vitro* models by incorporating multiple cell types into scaffold-free tumor tissues with defined architecture. We generated tumor tissues from distinct subtypes of

[*]Correspondence: searsr@ohsu.edu.

AUTHOR CONTRIBUTIONS

E.M.L., B.L.A.-P., and S.M.K. designed, performed, and analyzed experiments; N.D.K., M.A.T., G.M.K., and T.S.A. performed experiments; R.S. and S.L.J. performed the SHG imaging; R.R. and J.L.M. performed the CLARITY experiments; B.C.S. provided de-identified primary patient tissue; G.T. and Y.H.C. performed image analysis; J.E.K., J.W.G., S.C.P., D.G.N., and R.C.S. designed and analyzed experiments; E.M.L., B.L.A.-P., S.M.K., and R.C.S. wrote the manuscript.

DECLARATION OF INTERESTS

The authors declare that S.M.K., S.C.P., and D.G.N. are employees and shareholders of Organovo Holdings, Inc. E.M.L., B.L.A.-P., and R.C.S. are inventors of technology that is utilized in this research and that has been optioned to Organovo, Inc. by OHSU. This potential conflict of interest has been reviewed and managed by OHSU.

SUPPLEMENTAL INFORMATION

Supplemental Information includes seven figures, two tables, and two datasets and can be found with this article online at https://doi.org/10.1016/j.celrep.2018.12.090.

breast or pancreatic cancer in relevant microenvironments and demonstrate that this technique can model patient-specific tumors by using primary patient tissue. We assess intrinsic, extrinsic, and spatial tumorigenic phenotypes in bioprinted tissues and find that cellular proliferation, extracellular matrix deposition, and cellular migration are altered in response to extrinsic signals or therapies. Together, this work demonstrates that multi-cell-type bioprinted tissues can recapitulate aspects of *in vivo* neoplastic tissues and provide a manipulable system for the interrogation of multiple tumorigenic endpoints in the context of distinct tumor microenvironments.

In Brief

Langer et al. use three-dimensional bioprinting to incorporate multiple cell types, including patient-derived cells, into scaffold-free *in vitro* tumor tissues. They show that cells within these tissues self-organize, secrete extracellular matrix factors, and respond to extrinsic signals and that multiple tumorigenic phenotypes can be assessed simultaneously.

Graphical ABSTRACT

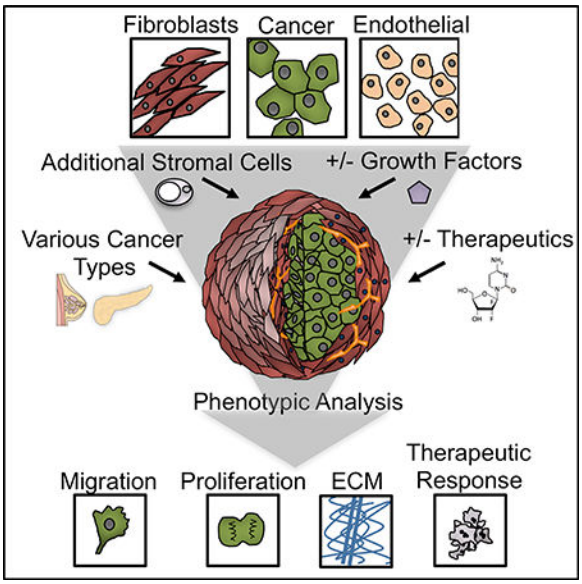

INTRODUCTION

Epithelial tumors initiate when cells deregulate the physiologic mechanisms that limit cell proliferation or induce cell death. The study of tumor cells in two-dimensional (2D) culture has revealed an understanding of genetic and epigenetic alterations that can initiate or contribute to cancer cell proliferation and other tumorigenic phenotypes (Hanahan and Weinberg, 2000, 2011). It has become clear, however, that tumor cells significantly impact the local tumor microenvironment, causing an expansion and activation of stromal cell types. In turn, stromal cells then generate a feedback loop, providing tumor cells with signals that contribute to oncogenic phenotypes, including proliferation, migration, and drug resistance (Hanahan and Coussens, 2012; Pietras and Ostman, 2010; Quail and Joyce, 2013). Distinct

microenvironments between or within tumors can also contribute to inter- and intratumoral phenotypic heterogeneity and differential drug response (Marusyk et al., 2012; Park et al., 2014; Plaks et al., 2015). Currently, standard *in vitro* tumor models lack cellular and spatial complexity, providing an overly simplistic view of tumor biology, which may contribute to the high attrition rate of candidate compounds in clinical trials (Hutchinson and Kirk, 2011). To understand the mechanisms underlying these complex tumor-stroma interactions, as well as their impact on tumorigenic phenotypes, it has become clear that improved multicellular *in vitro* models are needed.

The field of tissue engineering, including the use of three-dimensional (3D) bioprinting to generate complex tissues, has seen rapid advances in recent years toward modeling both normal tissues and disease states (Khademhosseini and Langer, 2016; Madden et al., 2018; Mandrycky et al., 2016; Ozbolat and Hospodiuk, 2016; Peng et al., 2016; Vanderburgh et al., 2016; Zhang et al., 2016a). 3D bioprinting allows for the generation of tissues that incorporate a variety of cell types in a complex and defined spatial architecture. Here, we tested whether 3D bioprinting could be used to generate multicellular, architecturally defined, scaffold-free tissue models of human tumors. We used Organovo's Novogen MMX Bioprinter Platform to print structures composed of a cancer cell core surrounded by several stromal cell types. We found that within these tissues, the cancer cells are exposed to signals from multiple cell types and that as the tissues matured, cells deposited extracellular matrix (ECM) and self-organized. We show that this system is compatible with the inclusion of diverse stromal and tumor cell types, including primary patient and patient-derived tumor tissues. Importantly, we assess a variety of tumorigenic phenotypes, including cell signaling, proliferation, ECM deposition, and cellular migration within these tissues in response to extrinsic signals or therapies. Together, we demonstrate a robust and manipulable in vitro model of human tumors that can be used to interrogate tumorigenic phenotypes in the context of complex tumor-stroma interactions.

RESULTS

3D Bioprinting Allows for Generation of Tumor Models That Include Multiple Cell Types in a Defined Spatial Architecture

Because the stroma plays a profound role in tumorigenic phenotypes, we sought to develop a robust *in vitro* model that incorporates both tumor and stromal cell types in a defined architecture and could be used to assess multiple tumorigenic phenotypes. To this end, we used Organovo's Novogen MMX Bioprinter Platform, which through continuous deposition technology deposits "bioink" (cells and/or cell-laden biomaterials) in a spatially defined architecture to build complex tissues (King et al., 2017; Nguyen et al., 2016b). We designed a tumor tissue model similar to solid tumor architecture in which a core tumor cell bioink was surrounded on all sides by a normal stromal cell bioink (Figure 1A). The bioink in each case included tunable hydrogels that were thermally and/or chemically modified to provide tensile strength and rigidity during tissue fabrication, but then they were removed during subsequent culture, leaving a purely cellular structure. These bioprinted tissues measured approximately 2 mm × 2 mm × 1 mm (Figure 1B), could be rapidly and reproducibly printed onto transwell membranes, and could be cultured in standard tissue culture conditions

(Figure 1C). Consistent with our bioprint design, 24 h after printing when the hydrogel is still present, cancer cells were constrained to the central core of the tissue (Figure 1D).

To begin modeling breast tumors, we bioprinted tumor tissue containing the estrogen receptor (ER)-positive MCF-7 cell line, primary human mammary fibroblasts (HMFs), and human umbilical vein endothelial cells (HUVECs). Structures were fixed on days 7 and 10 post-print, and H&E staining was performed on formalin-fixed paraffin-embedded (FFPE) sections. Structures showed tissue-like cellular density and close interaction of epithelial and stromal cell types (Figure 1E). The MCF7 cancer cells within these tissues were predominately found in the center of the structure and surrounded by stroma, similar to the original scripted spatial organization (Figures 1E-1G). Masson's trichrome staining showed the presence of collagen fibers predominantly in the stromal compartment, with increased staining at day 10 versus day 7, indicating that the cells within the tissues are depositing their own ECM and maturing over time (Figure 1F). Immunofluorescence staining confirmed close interaction between epithelial cancer cells (Cytokeratin 8/18 [KRT8/18] positive) and stromal fibroblasts (vimentin [VIM] positive) (Figure 1G). In addition, endothelial cells within the bioprinted tissues, visualized with a CD31 (PECAM1) antibody, self-organized into capillary-like networks (Figure 1G). To determine if endothelial cells were capable of forming complex contiguous networks, we used the CLARITY technique along with light-sheet microscopy (Chung et al., 2013) to visualize endothelial cells throughout the bioprinted tumor tissue. Endothelial cells (CD31+) formed intact networks with multiple branch points that traversed across the tissue (Figure 1H). Finally, we subcutaneously implanted day 10 tissues containing MDA-MB-231 breast cancer cells into immunocompromised mice and found that cancer cells within bioprinted tissues retained their tumorigenic properties and grew as xenografts (Figure S1). Together, these data show that bioprinted epithelial and stromal cell types are able to survive, self-organize, and interact with one another to form tissue-like structures.

Bioprinted Tissues Can Model Distinct Tumor Cell Subtypes

Tumor cell heterogeneity can result from differences in cell intrinsic (e.g., genetic) or extrinsic (e.g., microenvironmental) signals received by tumor cells, and such heterogeneity has been shown to affect tumorigenic phenotypes, such as growth, metastatic capacity, and/or therapeutic response (Brooks et al., 2015; Brooks and Wicha, 2015; Marusyk et al., 2012; Polyak, 2011). To determine if bioprinted tissues could be broadly applied to study tumor heterogeneity, we first tested whether they could model multiple human breast cancer subtypes (Prat et al., 2010; Sørlie et al., 2001). We bioprinted breast cancer cell lines from distinct subtypes, including luminal (MCF-7), HER2 amplified (SKBR3), basal-like (HCC1143), and claudin low (MDA-MB-231), all of which were able to form healthy tissues (Figures 2A-2C). To track the growth of the cancer populations over time, we infected each cell line with a lentivirus encoding firefly luciferase and added D-luciferin substrate to the tissues at days 4, 7, and 10 to quantify luminescence for each of the breast cancer subtypes. We found that MCF-7, SKBR3, and HCC1143 cell lines displayed modest or no increase in cell number over this time course (Figure 2D). In contrast, the MDA-MB-231 cell line grew rapidly, significantly increasing luciferase readout by about 7-fold on day 10 compared to day 4 (Figure 2D). To confirm this result, we also performed Ki67

staining of tissues on days 4, 7, and 10 and quantified the percentage of proliferating cancer cells (Ki67 and KRT8/18 double-positive cells; see Data S1) for each subtype (Figures 2E, S2A, and S2B). Consistent with the luciferase data, we found that MDA-MB-231 cells had a significant increase in the percentage of Ki67-positive cancer cells at both days 7 and 10. Similar results were seen in independent experiments analyzed only at day 10 (Figure S2B). The fibroblasts within bioprinted tissues displayed much lower proliferation than the cancer cells (Figure S2C). Finally, we compared the Ki67 staining in the bioprinted tissue to that of the cancer cells growing in traditional 2D culture and found that, in contrast to bioprinted tissues, cell lines grown in 2D displayed much higher Ki67 positivity (Figure 2F; see Table S1 for quantification scripts). Together, these data suggest that the proliferative capacity of cancer cell lines is altered in the context of the complex microenvironment within bioprinted tissues.

Within bioprinted tissues containing MDA-MB-231 cells, which have been shown to be highly invasive and metastatic *in vivo* (Cailleau et al., 1978; Minn et al., 2005a; Minn et al., 2005b), the cancer cells that were printed into the central pocket were found to rapidly migrate into and disperse among the stromal cells. To quantify this dispersal, we stained bioprinted tissues from all four breast cancer lines printed on the same day with KRT8/18 and VIM. Image analysis (see Data S2) was performed to calculate a cancer cell closeness centrality score (CCS) (Huang and Wang, 1995; Li and Lee, 1993; Otsu, 1979; Serra, 1979), where high numbers indicate close proximity of cancer cells to each other and low numbers indicate migration and dispersal throughout the tissue (Figure S3A). We found SKBR3 cells to have the highest CCS of the four lines as they retain a strict central location within the tissues, whereas MDA-MB-231 cells have the lowest CCS score, consistent with these cells migrating away from the center of the tissues (Figure 2G). In addition to analyzing the proliferation and migration of the cancer cells, we also analyzed collagen deposition by trichrome staining (see Table S2) and endothelial network formation by CD31+ staining in the printed tissues from each subtype (Figures S3B and S3C). MDA-MB-231-containing tissues had significantly less collagen deposition compared to the other breast cancer tissues (Figure 2H), but no significant differences were found in the endothelial network formation (Figure S3D). Together, these data indicate that bioprinted tissues can be used to evaluate interactions between cancer cell and the tumor microenvironment and provide a platform for analyzing the invasive phenotypes of cancer cells.

Distinct Microenvironments Can Be Modeled in Bioprinted Tissues

To evaluate the ability of bioprinted tissues to model different types of stromal microenvironments, we incorporated into the stromal mix additional cell types that have been shown to be present in human breast tumors and that affect tumor phenotypes. The interaction of breast cancer cells with adipocytes has been shown to result in more invasive phenotypes and drug resistance (Dirat et al., 2011). Therefore, we incorporated primary human subcutaneous preadipocytes (SPA) into the tissue stromal compartment along with HMFs and HUVECs and then matured the SPA cells by using well-characterized differentiation factors in the culture medium (Gregoire, 2001). Adipocyte maturation was verified by staining cryosections of bioprinted tissues with Oil Red O. Lipid droplets were found throughout the stromal compartment of the tissue (Figure S4A). To quantify adipocyte

maturation, conditioned medium collected daily from bioprinted tumor tissues was assessed for leptin, a hormone secreted by adipocytes. Leptin levels rose steadily over 10 days in culture, reaching approximately 600 pg leptin/mL in the culture medium at day 10 (Figure S4B). These studies demonstrate that additional tissue-relevant cell types can be included in the stromal microenvironment by the incorporation of stem-like precursor cells that can be then differentiated during the culture of bioprinted tissues.

In addition to cell types present in normal breast tissue, cells from the bone marrow can infiltrate into breast tumors and affect tumor growth and progression. One such cell type, bone-marrow-derived mesenchymal stem cells (MSCs), has been shown to secrete chemokines, cytokines, growth factors, and ECM proteins that drive increased proliferation and migration of tumor cells and help to establish a metastatic niche (Djouad et al., 2006; Karnoub et al., 2007; Shi et al., 2017; Zhu et al., 2006). To determine if our system is compatible with the inclusion of MSCs, we mixed primary human bone-marrow-derived MSCs into the stromal cell mix with HMFs and HUVECs. Tissues that included MSCs were healthy and displayed similar histologic appearance to the basic breast cancer prints (Figures 3A and S4C). Immunofluorescence analysis of these tissues at day 10 showed that both tissues contained a central cancer pocket (Figure 3B). Using luminescence readings over time, we found that +MSC structures had increased cancer cell numbers at day 4; however, by day 10 there was no significant difference between conditions (Figure 3C). Consistent with these results, there was no significant difference in the percent of Ki67-positive cells, either epithelial (KRT8/18+) or stromal (VIM+), between these tissues at days 4, 7, and 10 (Figures 3D and S4D). An analysis of cell migration in these tissues also revealed no significant change in the CCS in the presence of MSCs (Figure S4E). We next assessed the ECM deposition with trichrome staining and found that although trichrome staining increases over time in tissues printed with and without MSCs, there was a significant increase in the deposition of collagen in bioprinted tissues containing MSCs at each time point, indicative of a more reactive and desmoplastic tumor microenvironment (Figures 3E and 3F). Consistent with these results, MSC-containing structures had increased expression of *COL1A1* and *COL1A2* but not *COL4A1* mRNA (Figure 3G). To determine whether the collagen present was matured into fibrils, we performed second harmonic generation (SHG) imaging and found that bioprinted tissues containing MSCs had increased mature collagen (Figure 3H). Together, these results are consistent with literature showing that MSCs contribute to a reactive, ECM-rich tumor microenvironment and indicate that bioprinted tissues can be used to model such phenotypes in heterotypic tumor tissue.

Bioprinted Tumor Tissue Can Be Use to Assess Therapeutic Efficacy

To evaluate whether culturing cells in 3D bioprinted tissues would affect sensitivity to chemotherapy compounds, 3D tissues printed with HMF, HUVEC, SPA, and MCF-7 cells or 2D co-cultures of the same four cell types were dosed daily for 3 days and assessed for metabolic activity by the CellTiter Glo ATP utilization assay. Upon doxorubicin treatment, the 3D tissues exhibited an LD_{50} value of 0.66 μM, as compared to 0.032 μM for 2D co-cultured cells (Figure 4A). Because the 2D co-culture contained the same cell types at the same ratio in close proximity, the 20-fold increase in resistance in 3D is likely not due to simple paracrine signaling but may instead reflect the impact of ECM and/or cancer cell

organization in the 3D tissues. Although paclitaxel was not fully efficacious in either 2D co-culture or 3D bioprinted tissues, the maximum efficacy in the 2D co-cultures was achieved with doses as low as 10 nM, whereas paclitaxel exhibited little to no toxicity on 3D tissues until doses reached 50 μM (Figure 4A).

To test the use of targeted therapies on cancer cells within bioprinted tissue, we bioprinted tissues containing HCC1143 cells and treated the tissues daily starting at day 4 with or without BEZ235, a phosphatidylinositol 3-kinase (PI3K)/mammalian target of rapamycin (mTOR) inhibitor. BEZ235 treatment was found to significantly reduce the phosphorylation of the S6 ribosomal protein, a readout of mTOR activity, throughout the tissues in both cancer and stromal cells (Figures 4B and S5). We quantified Ki67 staining in the HCC1143-containing bioprinted tissues treated with and without BEZ235 and found that despite decreased phospho-S6 ribosomal protein (pS6), there was no significant decrease in the percent of Ki67-positive cancer cells (Figure 4C). To determine if this lack of therapeutic response in 3D was due to the presence of paracrine signals from fibroblasts, we grew HCC1143 cells in 2D culture with increasing concentrations of HMF-conditioned medium and then treated with either vehicle or BEZ235. In normal growth conditions (no conditioned medium), BEZ235 reduced the number of Ki67-positive cells by ~50% (Figure 4D). The efficacy of BEZ235 treatment was significantly reduced with the addition of fibroblast-conditioned medium (Figure 4D), suggesting that paracrine factors from these cells contribute to BEZ235 therapeutic resistance in bioprinted tissues.

Bioprinted tissue contains multiple cell types, suggesting that this model would also allow for the analysis of therapeutics targeting stromal cells. Because the endothelial cells in these tissues organize into vascular-like networks, we treated bioprinted tissues with Sunitinib, a multi-targeted receptor, tyrosine kinase, used to reduce angiogenesis through vascular endothelial growth factor receptor (VEGFR) inhibition in tumors. We bioprinted tissues containing different breast cancer cell lines as in Figure 2 and treated these tissues with or without Sunitinib. Sunitinib dramatically reduced the endothelial cell networks within these tissues (Figures 4E and 4F). Aguilera et. al. demonstrated that anti-VEGF therapy can promote tumor aggressiveness at least in part through increasing collagen deposition (Aguilera et al., 2014). To determine if Sunitinib treatment increased collagen deposition, we analyzed MDA-MB-231 bioprinted tissues, which contain relatively low basal levels of collagen (see Figures 2B and 2H). Following Sunitinib treatment, MDA-MB-231 tissues displayed a dramatic increase in trichrome staining (Figure 4G). Importantly, a significant increase in collagen deposition was also observed in *in vivo* orthotopic xenografts of MDA-MB-231 cells treated with Sunitinib (Figure 4H). Together, these results support the use of bioprinted tissues to simultaneously interrogate the impact of therapeutic compounds on both cancer and stromal compartments and suggest that bioprinted tissues can recapitulate *in vivo* phenotypes.

3D Bioprinting Can Model Additional Tumor Types, Including Pancreatic Cancer

During pancreatic ductal adenocarcinoma (PDA) progression there is a large expansion of the tumor microenvironment, which can ultimately comprise up to 90% of the tumor mass and significantly contribute to progression and therapeutic resistance (Neesse et al., 2011).

The growth of pancreatic cancer cells in 2D culture lacks the complex cellular interactions necessary to model this aggressive disease; therefore, there is a critical unmet need for more appropriate laboratory models of PDA. We examined whether the growth of pancreatic cancer cells in bioprinted tissue could recapitulate aspects of human pancreatic tumors. Primary patient tissue was obtained from the Oregon Pancreas Tissue Registry (OPTR), and OPTR3099C, a human pancreatic cancer cell line generated from patient-derived xenograft (PDX) tumor tissue, was printed in a stromal mixture of HUVECs and normal human primary pancreatic stellate cells (PSCs), fibroblast-like cells that are thought to be responsible for the dense desmoplastic reaction found in PDA patients (Figure 5A). Similar to the bioprinted breast cancer tissue, these low-passage PDA cells formed tissues with cancer cells (KRT8/18+) in a central location surrounded by an extensive network of HUVECs (CD31+) and PSCs (VIM+). At the cancer-stroma border, isolated stromal cells were found within the cancer region (Figure 5B, arrows), and, similarly, cancer cells could be seen forming intimate connections with endothelial cells in the stromal region (Figure 5B, arrow heads and inset). Cancer cells within these tissues maintained proliferative capacity (Ki67+) (Figures 5C and S6A). Implantation of PDA bioprinted tissues containing a human pancreatic cancer cell line, HPAFII, into NSG mice led to robust tumor formation *in vivo* (Figures S6B and S6C). Activation of PSCs occurs in response to injury, inflammation, or tumorigenesis, leading to increased proliferation and deposition of ECM by these cells (Sherman, 2018). We found that bioprinted PSCs express alpha-smooth muscle actin (aSMA), a marker of activation, and exhibit dense directionality, as seen in desmoplastic tumors (Figure 5D). In addition, these tissues contained mature collagen fibrils, as detected by SHG imaging (Figure 5E). Together these data suggest that, similar to patient tumors, PDA cells grown in bioprinted tissue are exposed to a dense, activated stroma.

To assess treatment efficacy in the PDA bioprinted tissues, we bioprinted HPAFII cells expressing firefly luciferase into a stromal bioink of PSCs and HUVECs and treated with gemcitabine, a standard of care chemotherapy. HPAFII cells belong to the classical subtype of PDA, which has been reported to have improved patient outcomes (Bailey et al., 2016; Collisson et al., 2011). These tissues were treated on day 4 with gemcitabine at a final concentration of 0, 10, or 50 μM. Luminescence was measured on day 10. In both the immunofluorescence (Figure 5F) and the luminescence reading (Figure 5G), we observed a dose-dependent response of cancer cell death with gemcitabine treatment.

Bioprinted Tumors Display Both Cancer and Stromal Cell Responses to Extrinsic Signals

Given that signaling within the tumor microenvironment can impact stromal and cancer cell phenotypes in human tumors, we wanted to examine cellular responses within bioprinted tissues to extrinsic signals known to alter tumor phenotypes *in vivo*. We treated bioprinted pancreatic cancer tissues with transforming growth factor β (TGFβ), a well-studied cytokine that activates PSCs, thereby inducing proliferation (Apte et al., 1999; Jaster, 2004). We found that TGFb treatment increased the cellular density of the tissue, which was consistent with a role for TGFβ in activation and subsequent increased proliferation of pancreatic stellate cells (Figures 6A and 6B). In addition to PSC activation, TGFβ can affect tumor cell intrinsic migratory capacity (Massagué, 2008). An assessment of the untreated tissues

revealed that the majority of tumor cells remained within the central region, consistent with the well-differentiated nature of HPAFII PDA cells. In contrast, tissues treated with TGFβ had a disrupted border and a significant percentage of HPAFII cancer cells had migrated into the surrounding stroma (Figures 6C and 6D).

Bioprinted Tissues Generated from Primary Patient Tumors Recapitulate *In Vivo* Morphology

After finding that established and patient-derived PDA cell lines survive and proliferate when printed into a base pancreatic stromal mix composed of HUVECs and PSCs (Figure 5), we next sought to determine whether we could print primary patient tissue for analysis of downstream endpoints, such as morphology and therapeutic response. Primary de-identified tumor tissue was obtained through the OPTR and was used to generate bioprinted tissue and/or PDX tumor tissue (see STAR Methods). Tumor tissue from patient OPTR4086 was enzymatically disassociated and bioprinted as the cancer cell bioink surrounded by the stromal bioink mixture of HUVECs and PSCs. Bioprinted tissues were harvested after 6–10 days of culture. Bioprinted cytokeratin-expressing cancer cells maintained higher order structure, with some regions displaying a cuboidal organization surrounding a lumen (Figure 7A). This morphology was similar to structures found in the primary patient tissue and PDX tumor tissue of this patient (Figures 7B and 7C). Furthermore, cells of the primary bioprinted tissue maintained E-cadherin+ cell-cell junctions and proliferative capacity, as determined by Ki67+ staining (Figure 7D).

The expansion of human tissue by using PDXs provides a renewable resource of human cancer cells that lack the cellular adaptation that occurs during growth on plastic. It has been shown in several tumor types that PDX tumors often are histologically and phenotypically similar to the primary tissue (Delitto et al., 2015), but these models are expensive and lack human stromal cells. To determine if we could use patient-derived cells from PDX models as the cancer bioink in bioprinted tissues and whether the bioprinted tissues that contain human stromal cells would display similar morphology and architecture to the *in vivo* tumors, we disassociated whole PDX tumors and printed the cell mixture into the base pancreatic stromal mix of HUVECs and PSCs. The resulting bioprinted PDX tissues maintained a similar morphology not only to the PDX tumor but also to the matching primary patient tumor (Figure 7E), suggesting that the 3D orientation of cells in bioprinted tissue allows for spatial organization similar to that of *in vivo* tissues. Within the bioprinted tissues, the majority of fibroblasts within the stromal compartment are human pancreatic stellate cells, as determined by positive expression for the human marker KU80 (Figure S7A). However, a minority population of VIM-positive and KU80-negative fibroblasts exists, suggesting that a small population of cancer-associated fibroblasts originating from the mouse host do survive throughout culture of bioprinted tissues (Figure S7A). Furthermore, the cancer cells were able to recapitulate signaling heterogeneity, as observed with pS6 staining, a readout of mTOR signaling, across primary, PDX, and disassociated PDX bioprinted tissues (Figures 7F and S7B). Stromal cells within bioprinted tissues exhibited low pS6 staining near the cancer core and high pS6 staining near the tissue edge, likely due to the availability of nutrients in the culture medium. In contrast, cancer cells (KRT8/18+) at the core of the bioprinted tissues exhibited heterogeneous pS6 staining, similar to that seen in patient and

PDX tumors (Figure 7F and S7B), which is consistent with the mTOR pathway being aberrantly activated in a large percentage of pancreatic cancer patients (Bellizzi et al., 2010). To determine the levels of proliferation, we analyzed Ki67-positive cells in bioprinted tissues containing disassociated PDX tissue and compared this to the matching *in vivo* PDX or primary patient tumor tissue. Consistent with our results in breast cancer cell lines (Figures 2, 3, and 4), cancer cells within the bioprinted tissues had proliferation rates comparable to both the PDX and primary patient tissue (Figure 7G). Finally, in contrast to HPAFII-containing bioprinted tissues, which showed a reduction in viability at 10 μM gemcitabine (see Figure 5), we detected large numbers of cancer cells even at high concentrations of gemcitabine (100 μM, double the peak plasma concentration [Abbruzzese et al., 1991]) in the bioprinted tissues generated from disassociated PDX tissue (Figures 7H-7J and S7C), suggesting that bioprinted tissue could represent a test platform for therapeutic sensitivity.

DISCUSSION

Accurate models of human tumors are needed to understand how complex tumor-stromal interactions contribute to tumor growth, progression, and therapeutic response. Genetically engineered mouse models and xenografts of cancer cells into immunocompromised mice have allowed for the study of tumors in the presence of a tumor microenvironment, but these models are costly, time consuming, do not include human stroma, and can be difficult to manipulate. Several advances have been made to *in vitro* culturing methods in attempts to better recapitulate the complex *in vivo* tumor microenvironment (Jaganathan et al., 2014; Katt et al., 2016; Longati et al., 2013; Park et al., 2014). Scaffold-based models, such as collagen or Matrigel, or scaffold-free heterotypic co-culture models, including multicellular tumor spheroids, allow for the integration of additional cell types into 3D culture. Compared to growth in 2D systems, cancer cells grown in these 3D environments have been shown to have significantly altered gene expression profiles and tumorigenic phenotypes, including proliferation and drug response, highlighting the importance of these cellular interactions to oncogenesis. (Fong et al., 2016; Stadler et al., 2015; Weigelt et al., 2014).

3D bioprinting has been used in a variety of approaches in an attempt to generate cancer models with a spatially defined architecture (Grolman et al., 2017; Zhang et al., 2016b; Xu et al., 2011; Zhao et al., 2014). Although these bioprinting approaches have advanced our knowledge of cellular behavior within a 3D system, most of these systems do not generate purely cellular models that are large scale (over 500 μm) with tissue-like organization. We tested whether 3D bioprinting could be used to create relatively large, complex, heterotypic, spatially defined, and purely cellular tumor tissue that incorporates both cancer and stromal cell types in a defined spatial orientation. We demonstrate that bioprinted tissues can be reproducibly generated using multiple cell types relevant to *in vivo* cancer biology. Similar to *in vivo* tumors, cancer cells within bioprinted tissues are surrounded by a microenvironment containing multiple stromal cell types, which allows for dynamic cell-cell interactions over time. During maturation of the bioprinted tissues, we observed phenotypic alterations in the stromal compartment, including ECM deposition, organization of endothelial cells into extensive networks, and directionality of stromal cells similar to the “rivers” of stroma seen in desmoplastic tumors, thereby recapitulating several characteristics of an *in vivo* tumor microenvironment.

The tumor microenvironment in 3D bioprinted tissues can be directly manipulated with the addition of multiple relevant stromal cell types, including adipocytes that secreted factors, such as leptin, into the microenvironment, or MSCs that increased collagen deposition and maturation within the tissues. Additional stromal cell types, such as immune cells or cell types found in metastatic microenvironments, for example, could be used in future studies. Modeling cancer in a controlled system with matched stromal cell composition allows for mechanistic investigations of subtype-specific tumor-stromal crosstalk that influences tumor phenotypes, such as ECM deposition. We found that different types of cancer cells vary in their ability to influence the surrounding stroma, as observed by a decrease in trichrome staining in tissues that included MDA-MB-231 cells compared to other breast cancer subtype cell lines. This line has previously been shown to be highly metastatic and, as such, expresses high levels of MMPs that degrade collagens (Bachmeier et al., 2001). In addition, the ability of endothelial cells to self-organize within bioprinted tumor tissues provides a platform to study not only the interactions between the endothelial and tumor cells but also the spatial organization of vascular networks within the tumor microenvironment and perturbagens that disrupt this organization. Consistent with *in vivo* studies, treatment of bioprinted tissues with the anti-VEGFR therapeutic agent Sunitinib significantly reduced endothelial networks and increased collagen deposition (Aguilera et al., 2014). These results support the use of bioprinted tissues to interrogate the effect of therapeutics on stromal phenotypes.

Due to the cellular complexity and *in-vivo*-like tissue architecture, bioprinted tissues can be used to assess the effect of a complex microenvironment on cancer cell proliferative capacity. In contrast to cells grown in 2D culture, we generally observed only a small percentage of Ki67-positive cancer cells in bioprinted tissue. Importantly, the proliferation rates observed in bioprinted tissues are similar to those seen in breast cancer patients (average of 10%–30%), indicating that these tissues may more accurately model *in vivo* therapeutic response, as non-dividing cells are often more resistant to therapies (Nishimura et al., 2010). Indeed, we found that the chemotherapies doxorubicin and paclitaxel were less effective in these 3D tissues than in 2D culture. In addition, we found that MDA-MB-231 cells grew rapidly within printed tissues, whereas MCF-7, SKBR3, and HCC1143 cell lines had modest, low growth during the 10-day time course, despite all having relatively high proliferation in 2D culture.

To further interrogate therapeutic response in heterotypic tissues, we tested the use of the targeted PI3K/mTOR inhibitor BEZ235 on HCC1143 bioprinted tissues and showed on-target effects with decreased pS6 staining in both stromal and cancer cells following treatment. Although BEZ235 was able to effectively shut down target signaling, PI3K/mTOR inhibition did not alter proliferation rates within bioprinted tissues. Together with the result that fibroblast-conditioned medium partially abrogated the effects of BEZ235 in 2D culture, these results suggest that secreted factors derived from fibroblasts provide resistance to mTOR inhibition and that such resistance phenotypes can be modeled in bioprinted tissues. In our HPAFII bioprinted tissues, we observed a dose response to gemcitabine treatment but did not completely eliminate the cancer population even at high therapeutic doses. In comparison, using PDA PDX bioprinted tissue, we observed substantial resistance

to gemcitabine. Together, these results suggest that bioprinted tissues could be used for studies of drug response and analysis of cytostatic versus cytotoxic effects of therapeutics.

The spatial orientation of cells within the bioprinted tissues allows for the investigation of tumorigenic phenotypes, such as cell migration, as well as an analysis of spatial heterogeneity. We observed increased proliferation and invasion of the MDA-MB-231 cells in bioprinted tissue compared to tissues printed with MCF7, SKBR3, and HCC1143 cell lines. This result is consistent with this cell line having aggressive and invasive growth characteristics, as evidenced in multiple other *in vitro* and *in vivo* systems (Cailleau et al., 1978; Minn et al., 2005a; Minn et al., 2005b). To assess whether 3D bioprinted tissues can model extrinsic signal-induced invasion into a 3D space, we treated bioprinted tissue containing HPAFII pancreatic cancer cells, which normally maintain a defined central location throughout the time course of growth, with TGFβ, a factor that regulates stellate cell activation, proliferation, and migration (Apte et al., 1999; Jaster, 2004; Massagué, 2008). The addition of TGFβ disrupted the tumor-stromal border, increasing the migration of pancreatic cancer cells, and increased the stromal density. Future studies will dissect the relative contribution of cancer cell-intrinsic or cell-extrinsic effects contributing to the migratory phenotypes. Due to the relatively large size and defined architecture of these bioprinted tissues, the ability of cancer cells to migrate hundreds of microns to the structure edge can be evaluated, providing a manipulable model system to detect tumor invasion through mature tissue and to investigate the reciprocal molecular mechanisms underlying this phenotype.

Finally, we demonstrate that bioprinting allows for modeling of primary patient or patient-derived tissue in a complex microenvironment. We show that bioprinted tissues generated with disassociated PDX tumors have proliferation rates that are comparable to the corresponding PDX tumor and patient tumor and that these rates are low compared to most lines grown in 2D culture. This, along with other aspects of the 3D and heterotypic microenvironment, suggests that cancer cells grown in bioprinted tissues may more accurately model *in vivo* phenotypes and, therefore, may more accurately model therapeutic response. In the future, bioprinted tissues containing cells from patient tumors with known clinical therapeutic response could be used to evaluate a prognostic use of bioprinted tumor tissue. Additionally, the ability to independently alter the cancer and stromal cell composition of bioprinted tissues will allow for the inclusion of patient-matched stromal cell types. We showed in the PDX bioprints that only a small proportion of the stromal cells in the print on day 7 are of mouse origin. Going forward, however, it will be possible to sort the cancer cells and print them with a pure population of either naive or tumor-educated human stroma. Together, these results demonstrate that bioprinted tissues provide a complex model system to interrogate both intrinsic and extrinsic signals from diverse cell types in a defined spatial organization. The flexibility of this system, including the ability to manipulate cells prior to printing, will facilitate mechanistic studies of the microenvironmental influence on tumor phenotypes and allow for patient-specific models of tumor biology.

STAR★METHODS

CONTACT FOR REAGENT AND RESOURCE SHARING

Further information and requests for resources and reagents should be directed to, and will be fulfilled by, the Lead Contact, Dr. Rosalie Sears (searsr@ohsu.edu).

EXPERIMENTAL MODEL AND SUBJECT DETAILS

Cell Culture—All primary cultures and cell lines were grown in standard tissue culture conditions at 37°C with 5% CO_2. Sources, catalog numbers, and sex for all cells are listed in the Key Resources Table. Sex of purchased primary cells is listed if known. Primary human mammary fibroblasts and primary human adult pulmonary fibroblasts were purchased from ScienCell (Carlsbad, CA) and cultured in fibroblast medium (ScienCell). Primary human pancreatic stellate cells (PSCs) and bone marrow-derived mesenchymal stem cells (MSCs) were purchased from ScienCell and cultured in PaSC media or MSC media (ScienCell), respectively. Human umbilical vein endothelial cells (HUVEC) were purchased from BD Biosciences (San Jose, CA) and cultured in EGM-2 media with EBM-2 supplements (Lonza, Basel, Switzerland) or from MilliporeSigma (Burlington, MA) and cultured in PeproGrow MacroV media (Peprotech, Rocky Hill, NJ). Human pulmonary microvascular endothelial cells were purchased from ScienCell and cultured in Endothelial Cell Media (ScienCell). Primary human subcutaneous preadipocytes (SPA) were purchased from Zen-Bio (Research Triangle Park, NC) and cultured in subcutaneous preadipocyte media (Zen-Bio). MCF-7 cells were purchased from MilliporeSigma (St. Louis, MO) or ATCC (Manassas, VA) and cultured in DMEM supplemented with 10% FBS with or without 1% penicillin/streptomycin. HPAFII, MDA-MB-231, SKBR3, and A549 cells were purchased from ATCC and cultured in DMEM supplemented with 10% FBS. HCC1143 were purchased from ATCC and cultured in RPMI supplemented with 10% FBS. Cell line identity was confirmed with STR profiling.

Primary patient tissue—Primary patient tissue was collected through the Oregon Pancreas Tissue Registry (OPTR) with informed written patient consent (IRB approved, IRB00003609). De-identified tissue was assigned a study number (OPTR #) and utilized for relevant experiments (IRB00003330). For direct patient bioprinted tissues, resected pancreatic tumor tissue from OPTR4086 was disassociated in 1.25 mg/ml collagenase IV and 1mg/ml soy bean trypsin inhibitor for 45 minutes at 37°C, washed three times with PBS, and then resuspended at 1.5 $\times 10^8$ cells/mL for printing.

Animal models—All animal work was completed in accordance with IACUC approved procedures. Animals were housed with no more than 5 animals per cage and given free access to food and water. PDX tumors were generated similar to that described (Kim et al., 2009). For patient derived xenografts, a 2 mm^3 piece of primary pancreatic tumor tissue from OPTR3099 was coated in Matrigel and implanted subcutaneously into the flank of healthy 6-week-old NOD.Cg-*Prkdcscid Il2rgtm1Wjl/SzJ* (NSG) mice. Once the tumor reached 1.5 cm in diameter, tumors were harvested and serially passaged *in vivo*. Both male and female mice were used. Passage 5 PDX tissue from OPTR3099 was harvested, and some of the tissue was formalin fixed paraffin embedded for further analysis and the rest was

disassociated for printing, as described below. To generate a low passage cell line of OPTR3099 (OPTR3099C), passage 3 PDX tissue was disassociated and plated in 2D culture in DMEM 10% FBS. Cells were passaged for at least nine passages to eliminate non-epithelial populations and bioprinted tissue was generated with these established cells as described below.

Xenografts of bioprinted tissues were performed similar to the PDX protocol described above. Briefly, bioprinted tissue was coated in Matrigel (BD Biosciences), and implanted subcutaneously into the flank of NSG mice. Tumors were calipered over time and harvested at 1.5 cm in diameter. Tumor tissue was formalin fixed and paraffin embedded for subsequent histological analysis.

For xenografts of MDA-MB-231 cells, 1×10^6 cancer cells were resuspended in 50% DMEM + 50% Matrigel and were implanted orthotopically into the 4^{th} mammary fat pads of healthy, female 6–8 week old NSG mice. Mice were randomized into treatment arms and treated daily for 14 days by oral gavage with Vehicle (0.5% w/v carboxymethylcellulose, 1.8% w/v NaCl, 0.9% v/v benzyl alcohol, 0.4% v/v Tween 80) or with 40 mg/kg Sunitinib malate. Treatment began 14 days after xenograft and mice were euthanized 28 days after xenograft. Tumor pieces were fixed in formalin, embedded in paraffin, sectioned, and stained by Masson's Trichrome.

METHOD DETAILS

3D Bioprinting—3D bioprinted cancer tissues were fabricated using a Novogen MMX Bioprinter Instrument (Organovo Inc., San Diego, CA) using previously established protocols (King et al., 2017; Nguyen et al., 2016a; Nguyen et al., 2016b). The cells for each compartment (stromal or cancer) were combined and resuspended in hydrogel at 37°C to a final concentration of $1.5–2.0 \times 10^8$ cells/mL. The hydrogel was a reversibly cross-linkable, alginate-containing hydrogel comprising 1% Pronova UP LVG Sodium Alginate (NovaMatrix, Sandvika, Norway) and 6% gelatin (MilliporeSigma) in PBS. To generate tissues, the cancer and stromal bioink mixes were loaded into Hamilton syringes fitted with 250 μm needles and bioprinted onto individual 0.4 μm or 3.0 μm Transwell clear polyester membrane inserts (Corning 3470 and 353181, respectively; Costar, Corning, NY) to generate structures as depicted in Figure 1B. Tissues were briefly treated with a buffered solution containing calcium chloride in order to crosslink the alginate-containing hydrogel and then were cultured at 37°C in media containing supplements used to support each of the cell types included. Crosslinked tissues were treated with Alginate Lyase (MilliporeSigma) 48 hours after printing, and subsequent culture at 37°C allowed complete removal of the hydrogel. Tissues were maintained in culture for up to 14 days, with media exchanges every day. In the standard print, the stromal compartment contained 75% fibroblasts or stellate cells and 25% HUVECs while the cancer compartment contained 75% cancer cells and 25% HUVECs. When adipocytes were included in the print, the stromal compartment contained a small proportion (10%–25%) preadipocytes which were differentiated in situ to adipocytes by exposure to standard adipocyte differentiation media, and when BMD-MSCs were included in the print, the stromal compartment contained 50% HMFs, 25% MSCs, and 25% HUVECs. For the pancreatic primary tumor or PDX prints, all cells obtained from the

dissociated tumor were used as the cancer cell mix. Each bioprinted tissue contained approximately 2.5 $\times 10^5$ cancer cells surrounded by 1.7 $\times 10^6$ stromal cells. Any deviation in the printing methods is denoted in the individual figure legends.

Histology—For histological analysis, tissues were fixed in 2% paraformaldehyde (Electron Microscopy Sciences, Hatfield, PA) and paraffinembedded. H&E staining and Trichrome staining were performed with standard methods. Following fixation, tissues were dehydrated and infiltrated with paraffin by automated processing on a TissueTek VIP tissue processing system (Sakura Finetek USA, Inc., Torrance, CA). Some tissues were processed before dehydration by pre-embedding in HistoGel (Thermo Fisher, Carlsbad, CA). Tissues were sectioned at 5 mm for histological or immunofluorescent staining. H&E staining was performed either using standard procedures with Hematoxylin (Vector Laboratories, Burlingame, CA) and Eosin Y solution (MilliporeSigma) or were generated using a Leica Autostainer XL (Leica Biosystems, Buffalo Grove, IL) according to manufacturer's instructions. Masson's Trichrome staining was performed with either a connective tissue stain kit (Abcam, Cambridge, MA) or with Richard-Allan Scientific Masson Trichrome Kit (Thermo Fisher). For lipid staining, tissues were snap-frozen in OCT and processed for cryosectioning. Cryosections were stained with Oil Red O and counterstained with hematoxylin according to the manufacturer's instructions (MilliporeSigma). Images were acquired on an Aperio AT Scanscope with ImageScope software (Leica Biosystems) or on a Zeiss Axio Scan with Zeiss Zen software (Zeiss Microscopy, Thornwood, NY). Tiled images were digitally stitched by either ImageScope or Zen software to generate full scan images shown.

Immunofluorescence—Immunofluorescence was performed on FFPE sections of bioprinted tissues as previously described (Farrell et al., 2017). Cells grown in 2D culture were fixed in 2% paraformaldehyde, permeablized, blocked, and incubated with primary and secondary antibodies (Listed in Key Resources Table). Images of cells in 2D culture were acquired on an IN Cell Analyzer (GE Healthcare Life Sciences, Pittsburgh, PA) and analyzed with CellProfiler. Images of bioprinted tissue or xenograft sections were acquired on a Zeiss Axioscan with Zen software (Zeiss Microscopy).

CLARITY and light-sheet microscopy—Immunostaining and 3D imaging of intact tissues was achieved by the CLARITY method of tissue clearing and light sheet microscopy (Chung et al., 2013). For CLARITY images, human lung adenocarcinoma A549 cells were bioprinted with human pulmonary fibroblasts and human pulmonary microvascular endothelial cells using the standard bioprinting procedure described in the STAR Methods. Tissues were maintained in culture for 14 days, fixed for 6 days in the standard CLARITY hydrogel fixative (Chung et al., 2013), and then polymerized at 37°C for 3 hours under nitrogen gas. The fixed and polymerized tissues were then passively cleared for greater than 6 weeks at 37°C in 4% SDS, 200 mM Boric acid, pH 8.5. Prior to immunostaining, the clearing solution was removed by washing the tissues for 2 days in PBS with 0.1% Triton X-100 (PBST). Immunostaining was performed at room temperature with antibodies diluted in PBST. Samples were incubated in primary antibody for 2 days at room temperature, washed in PBST for one day, incubated in secondary antibody for 2 days, then washed again

in PBST for one day. For imaging, the samples were equilibrated in 85% glycerol in PBST for refractive index matching, then imaged in a Zeiss Lightsheet Z.1 microscope equipped with a Clr Plan-Neofluar 20×/1.0 objective (Zeiss Microscopy) and Zen Sp1 software, black edition (Zeiss Microscopy). Final 3D renderings and movies were generated using Imaris software, version 10 (Bitplane, Concord, MA).

Detection of secreted leptin—To assess maturation of adipocytes, conditioned media from tissues was collected and analyzed for leptin by ELISA according to the manufacturer's instructions (Thermo Fisher). Samples were analyzed on a BMG Labtech POLARstar Omega plate reader and compared to a standard curve (Cary, NC). Graphed data represent the average of triplicate tissues from triplicate experiments plus or minus standard deviation, with statistics calculated by one-way ANOVA with Dunnett's post-test versus day 1 using GraphPad Prism software (La Jolla, CA).

Treatment and therapeutic response studies—Doxorubicin and paclitaxel were acquired from MilliporeSigma. Tissues were dosed daily for three days beginning at day 4 of culture. Treated tissues were lysed by bead-based homogenization (QIAGEN, Hilden, Germany), and lysates assessed for ATP utilization by a Cell Titer Glo assay according to the manufacturer's instructions (Promega, Madison, WI). For comparison, a 2D co-culture comprising all 4 component cell types (NHMF, HUVEC, SPA, MCF7) mixed together at the ratio used for generating bioprinted tissues was treated for 72 hours and then similarly analyzed by the Cell Titer Glo assay (Promega). For both 3D and 2D experiments, data from triplicate samples from triplicate experiments were averaged and graphed as a nonlinear regression following transformation of compound concentrations to log values and normalization to vehicle control. All calculations were performed using GraphPad Prism software.

For assessment of cancer cell viability and proliferation within tissues, MCF-7, SKBR3, HCC1143, MDA-MB-231, and HPAFII cells were infected with lentivirus generated with the pLV416G vector (Collisson et al., 2011) to express both firefly luciferase and mCherry. Stable pools were selected in G418 containing media and mCherry expressing cells sorted on an InFlux cell sorter (BD Biosciences). To measure cancer cell viability and growth in tissues containing cells that express firefly luciferase, D-Luciferin (Perkin Elmer, Waltham, MA) was added to the transwell on the indicated days at a final concentration of 150 μg/mL. Luminescence was assessed on the IVIS Lumina XRMS *In Vivo* Imaging System (Perkin Elmer) 20 minutes after D-Luciferin addition.

Treatment with BEZ235 (SelleckChem, Houston, TX), gemcitabine (LC Laboratories, Woburn, MA), or Sunitinib (LC Laboratories) was started on day 4 of culture and dosed daily until tissues were fixed for analysis on day 10. TGFβ (Peprotech) was used at final concentration of 5 ng/mL beginning 24 hours after printing and was also dosed daily through day 10.

SHG imaging—For SHG imaging, 10 μm sections were deparaffinized, and mounted with CC/Mount mounting media (MilliporeSigma) and then with Richard-Allen Scientific Mounting Medium (Thermo Fisher). SHG imaging was performed on a custom SHG/Two-

Photon Fluorescence (SHG/TPF) microscope. A tunable Ti:Saphire (Griffin-C, KMLabs, Boulder, CO) femtosecond laser light source was tuned to 800 nm central wavelength with a bandwidth of 70 nm. The device is configured as a three-channel system to acquire two-photon epi- fluorescence (TPF), backward SHG (bSHG) and forward SHG (fSHG) signals. A narrow bandpass filter (Brightline Fluorescence Filter 390/40, Semrock, Inc. Rochester NY) was used to separate the bSHG signal from TPF signal and signals were acquired using two photon multiplier tubes (PMT) (H-7422, Hamamatsu Corporation, Japan). A 1.25 NA condenser lens collected the transmitted fSHG signal and was detected by a PMT (H5773, Hamamatsu Corporation). 2D scanning (x, y) was achieved using galvo mirrors (Nutfield Technology, Hudson, NH), and a piezo objective lens holder (MIPOS 500, Piezosystem, Jena, Germany) was used for axial scanning (z). The sample holder is mounted on a computer-controlled XY translational stage (Zaber technologies, Vancouver, BC) that enabled data acquisition from large tissue section (several millimeters in size) by acquiring a XY grid of images. The sample was coupled to a 20× objective lens (XLUMPLFLN 20XW, Olympus, Waltham, MA) using water. A grid of images was acquired covering the whole sample by translating the sample in a serpentine pattern using the XY translational stage. 3 images were acquired per grid element to generate a composite RGB image: Two-photon auto-fluorescence (green), bSHG (red) and fSHG (blue). The composite RGB image shown includes two-photon auto-fluorescence (green), backward SHG (bSHG, red) and forward SHG (fSHG, blue). The color of the collagen ranged from Red - > Purple - > Blue to represent the fraction of bSHG to fSHG signal from the collagen. The balance between the fSHG and bSHG signals is sensitive to the packing of collagen fibrils within the focus of the objective lens. The RGB composite image from grid elements was stitched using FIJI software to generate an image to display a complete 3D printed tissue section (Preibisch et al., 2009; Schindelin et al., 2012).

Quantitative RT-PCR—Day 7 MCF-7 breast cancer tissues bioprinted with or without BMD-MSCs in the stroma were used to assess RNA expression of Collagen genes. Briefly, RNA was isolated with the RNeasy kit with on-column DNase treatment. First strand synthesis was done according to the manufacturer's protocol with Multiscribe RT kit (Thermo Fisher) and qPCR was performed with Fast SYBR green on a StepOne machine. Primer sequences for *COL1A1*, *COL1A2*, *COL4A1*, and *TBP* are listed in the Key Resources Table (Bièche et al., 2003; Corsa et al., 2016).

QUANTIFICATION AND STATISTICAL ANALYSIS

For quantitation of Ki67 staining in the bioprinted tissues, we used a custom pipeline that first segmented nuclei and then estimated the cell boundaries by inflating the segmented nuclei by a 6 pixel ring to represent the cytoplasm (Data S1). The nuclei segmentation was performed using a succession of mathematical morphology operations as described (Serra, 1979). Briefly, a white top-hat was performed to detect the candidate nuclei and separated using a seeded watershed transformation from the ultimate eroded results. Next, marker segmentation using automatic thresholding techniques was performed to detect which nuclei/cells are positive for VIM, KRT8/18, and Ki67 (Huang and Wang, 1995; Li and Lee, 1993; Otsu, 1979). Cells with VIM or KRT8/18 staining in the cytoplasm were defined as

fibroblast or cancer cells, respectively. Cells with Ki67 staining in the nuclei were defined as Ki67 positive.

Ki67 staining quantitation for 2D tissue culture and xenografts was done using CellProfiler (Table S1). Briefly, nuclei were identified using Cell Profiler's automatic threshold strategy to distinguish from background in DAPI channel, and clumped nuclei were distinguished by shape. Ki67 positive nuclei were identified using the Otsu thresholding method for each previously identified nucleus.

For quantitation of cancer cell dispersal within the bioprinted tissues, we identified cancer and stromal cells based on marker expression (as described above) and used the cell location data (center of nucleus) from the cell segmentation output to characterize the spatial distribution of cancer cells (Data S2). First, we constructed an adjacency map using Delaunay triangulation, and then calculated weighted closeness centrality scores (CCS) (Newman, 2003), as the inverse sum of distances between the i-th cancer cell and all reachable cancer cells. Higher scores indicate that cells are more central to the main pattern of distances among all of the cells, lower values indicate that cells are more dispersed.

Collagen deposition was quantified from Trichrome stain using ImageJ (Schneider et al., 2012) modified from (Kennedy et al., 2006) (Table S2). Quantitation of CD31 staining in bioprinted tissues was performed using ImageJ by assessing the percent of CD31 positive area per high-powered field in each structure. Cell density was quantified as hematoxylin stained nuclei per high-powered field using ImageJ. Cancer cell migration in response to TGFb treatment was quantified using ImageJ as the percent area of mCherry positivity in the stromal region relative to total mCherry area in both the stromal and epithelial regions. The epithelial region was defined as the largest central region of VIM negative cells.

Statistical significance was determined using GraphPad Prism software with either a two-tailed Student's t test or a one-way or two-way ANOVA, as denoted in the figure legends. All graphs represent either the mean or a Tukey Boxplot ± SEM unless denoted in the figure legend. Significance, represented with asterisks, is defined as a p-value less than 0.05.

Supplementary Material

Refer to Web version on PubMed Central for supplementary material.

ACKNOWLEDGMENTS

The authors would like to thank Olivia A. Creasey for her contributions to this manuscript as well as Pamela Canaday and the Flow Cytometry Shared Resource at OHSU for sorting labeled cells used in these studies. The studies presented were funded by NIH R01 CA196228 (R.C.S.), NIH U54 grant CA209988 (R.C.S. and J.W.G.), SBIR phase I contract grant HHSN261201400024C (Organovo, Inc.), Collins Medical Trust (E.M.L.), as well as philanthropic support from Brenden-Colson Center for Pancreatic Care Program Leader Discovery Science Funding and Prospect Creek SMMART Trials. Flow cytometry work was performed in an OHSU Shared Resource supported by the Knight Cancer Institute through their NIH P30 grant CA69533.

REFERENCES

Abbruzzese JL, Grunewald R, Weeks EA, Gravel D, Adams T, Nowak B, Mineishi S, Tarassoff P, Satterlee W, Raber MN, et al. (1991). A phase I clinical, plasma, and cellular pharmacology study of gemcitabine. J. Clin. Oncol. 9, 491–498. [PubMed: 1999720]

Aguilera KY, Rivera LB, Hur H, Carbon JG, Toombs JE, Goldstein CD, Dellinger MT, Castrillon DH, and Brekken RA (2014). Collagen signaling enhances tumor progression after anti-VEGF therapy in a murine model of pancreatic ductal adenocarcinoma. Cancer Res. 74, 1032–1044. [PubMed: 24346431]

Apte MV, Haber PS, Darby SJ, Rodgers SC, McCaughan GW, Korsten MA, Pirola RC, and Wilson JS (1999). Pancreatic stellate cells are activated by proinflammatory cytokines: implications for pancreatic fibrogenesis. Gut 44, 534–541. [PubMed: 10075961]

Bachmeier BE, Nerlich AG, Lichtinghagen R, and Sommerhoff CP (2001). Matrix metalloproteinases (MMPs) in breast cancer cell lines of different tumorigenicity. Anticancer Res. 21, 3821–3828. [PubMed: 11911253]

Bailey P, Chang DK, Nones K, Johns AL, Patch AM, Gingras MC, Miller DK, Christ AN, Bruxner TJ, Quinn MC, et al.; Australian Pancreatic Cancer Genome Initiative (2016). Genomic analyses identify molecular subtypes of pancreatic cancer. Nature 531, 47–52. [PubMed: 26909576]

Bellizzi AM, Bloomston M, Zhou XP, Iwenofu OH, and Frankel WL (2010). The mTOR pathway is frequently activated in pancreatic ductal adenocarcinoma and chronic pancreatitis. Appl. Immunohistochem. Mol. Morphol 18, 442–447. [PubMed: 20661135]

Bièche I, Onody P, Tozlu S, Driouch K, Vidaud M, and Lidereau R (2003). Prognostic value of ERBB family mRNA expression in breast carcinomas. Int. J. Cancer 106, 758–765. [PubMed: 12866037]

Brooks MD, and Wicha MS (2015). Tumor twitter: cellular communication in the breast cancer stem cell niche. Cancer Discov. 5, 469–471. [PubMed: 25941337]

Brooks MD, Burness ML, and Wicha MS (2015). Therapeutic implications of cellular heterogeneity and plasticity in breast cancer. Cell Stem Cell 17, 260–271. [PubMed: 26340526]

Cailleau R, Olivé M, and Cruciger QV (1978). Long-term human breast carcinoma cell lines of metastatic origin: preliminary characterization. In Vitro 14, 911–915. [PubMed: 730202]

Chung K, Wallace J, Kim SY, Kalyanasundaram S, Andalman AS, Davidson TJ, Mirzabekov JJ, Zalocusky KA, Mattis J, Denisin AK, et al. (2013). Structural and molecular interrogation of intact biological systems. Nature 497, 332–337. [PubMed: 23575631]

Collisson EA, Sadanandam A, Olson P, Gibb WJ, Truitt M, Gu S, Cooc J, Weinkle J, Kim GE, Jakkula L, et al. (2011). Subtypes of pancreatic ductal adenocarcinoma and their differing responses to therapy. Nat.Med 17, 500–503. [PubMed: 21460848]

Corsa CA, Brenot A, Grither WR, Van Hove S, Loza AJ, Zhang K, Ponik SM, Liu Y, DeNardo DG, Eliceiri KW, et al. (2016). The action of discoidin domain receptor 2 in basal tumor cells and stromal cancer-associated fibroblasts is critical for breast cancer metastasis. Cell Rep. 15, 2510–2523. [PubMed: 27264173]

Delitto D, Pham K, Vlada AC, Sarosi GA, Thomas RM, Behrns KE, Liu C, Hughes SJ, Wallet SM, and Trevino JG (2015). Patient-derived xenograft models for pancreatic adenocarcinoma demonstrate retention of tumor morphology through incorporation of murine stromal elements. Am. J. Pathol 185, 1297–1303. [PubMed: 25770474]

Dirat B, Bochet L, Dabek M, Daviaud D, Dauvillier S, Majed B, Wang YY, Meulle A, Salles B, Le Gonidec S, et al. (2011). Cancer-associated adipocytes exhibit an activated phenotype and contribute to breast cancer invasion. Cancer Res. 71, 2455–2465. [PubMed: 21459803]

Djouad F, Bony C, Apparailly F, Louis-Plence P, Jorgensen C, and Noël D (2006). Earlier onset of syngeneic tumors in the presence of mesenchymal stem cells. Transplantation 82, 1060–1066. [PubMed: 17060855]

Farrell AS, Joly MM, Allen-Petersen BL, Worth PJ, Lanciault C, Sauer D, Link J, Pelz C, Heiser LM, Morton JP, et al. (2017). MYC regulates ductal-neuroendocrine lineage plasticity in pancreatic ductal adenocarcinoma associated with poor outcome and chemoresistance. Nat. Commun 8, 1728. [PubMed: 29170413]

Fong EL, Harrington DA, Farach-Carson MC, and Yu H (2016). Heralding a new paradigm in 3D tumor modeling. Biomaterials 108, 197–213. [PubMed: 27639438]

Gregoire FM (2001). Adipocyte differentiation: from fibroblast to endocrine cell. Exp. Biol. Med. (Maywood) 226, 997–1002. [PubMed: 11743135]

Grolman D, Bandyopadhyay D, Al-Enizi A, Elzatahry A, and Karim A (2017). Dual imprinted polymer thin films via pattern directed self-organization. ACS Appl. Mater. Interfaces 9, 20928–20937. [PubMed: 28562002]

Hanahan D, and Coussens LM (2012). Accessories to the crime: functions of cells recruited to the tumor microenvironment. Cancer Cell 21, 309–322. [PubMed: 22439926]

Hanahan D, and Weinberg RA (2000). The hallmarks of cancer. Cell 100, 57–70. [PubMed: 10647931]

Hanahan D, and Weinberg RA (2011). Hallmarks of cancer: the next generation. Cell 144, 646–674. [PubMed: 21376230]

Huang LK, and Wang MJJ (1995). Image thresholding by minimizing the measures of fuzziness. Pattern Recognit. 28, 41–51.

Hutchinson L, and Kirk R (2011). High drug attrition rates—where are we going wrong? Nat. Rev. Clin. Oncol 8, 189–190. [PubMed: 21448176]

Jaganathan H, Gage J, Leonard F, Srinivasan S, Souza GR, Dave B, and Godin B (2014). Three-dimensional in vitro co-culture model of breast tumor using magnetic levitation. Sci. Rep 4, 6468. [PubMed: 25270048]

Jaster R (2004). Molecular regulation of pancreatic stellate cell function. Mol. Cancer 3, 26. [PubMed: 15469605]

Karnoub AE, Dash AB, Vo AP, Sullivan A, Brooks MW, Bell GW, Richardson AL, Polyak K, Tubo R, and Weinberg RA (2007). Mesenchymal stem cells within tumour stroma promote breast cancer metastasis. Nature 449, 557–563. [PubMed: 17914389]

Katt ME, Placone AL, Wong AD, Xu ZS, and Searson PC (2016). In vitro tumor models: advantages, disadvantages, variables, and selecting the right platform. Front. Bioeng. Biotechnol 4, 12. [PubMed: 26904541]

Kennedy DJ, Vetteth S, Periyasamy SM, Kanj M, Fedorova L, Khouri S, Kahaleh MB, Xie Z, Malhotra D, Kolodkin NI, et al. (2006). Central role for the cardiotonic steroid marinobufagenin in the pathogenesis of experimental uremic cardiomyopathy. Hypertension 47, 488–495. [PubMed: 16446397]

Khademhosseini A, and Langer R (2016). A decade of progress in tissue engineering. Nat. Protoc 11, 1775–1781. [PubMed: 27583639]

Kim MP, Evans DB, Wang H, Abbruzzese JL, Fleming JB, and Gallick GE (2009). Generation of orthotopic and heterotopic human pancreatic cancer xenografts in immunodeficient mice. Nat. Protoc 4, 1670–1680. [PubMed: 19876027]

King SM, Higgins JW, Nino CR, Smith TR, Paffenroth EH, Fairbairn CE, Docuyanan A, Shah VD, Chen AE, Presnell SC, and Nguyen DG (2017). 3D proximal tubule tissues recapitulate key aspects of renal physiology to enable nephrotoxicity testing. Front. Physiol 8, 123. [PubMed: 28337147]

Li CH, and Lee CK (1993). Minimum cross entropy thresholding. Pattern Recognit. 26, 617–625.

Longati P, Jia X, Eimer J, Wagman A, Witt MR, Rehnmark S, Verbeke C, Toftgård R, Löhr M, and Heuchel RL (2013). 3D pancreatic carcinoma spheroids induce a matrix-rich, chemoresistant phenotype offering a better model for drug testing. BMC Cancer 13, 95. [PubMed: 23446043]

Madden LR, Nguyen TV, Garcia-Mojica S, Shah V, Le AV, Peier A, Visconti R, Parker EM, Presnell SC, Nguyen DG, et al. (2018). Bioprinted 3D primary human intestinal tissues model aspects of native physiology and ADME/Tox functions. iScience 2, 156–167. [PubMed: 30428372]

Mandrycky C, Wang Z, Kim K, and Kim DH (2016). 3D bioprinting for engineering complex tissues. Biotechnol. Adv 34, 422–434. [PubMed: 26724184]

Marusyk A, Almendro V, and Polyak K (2012). Intra-tumour heterogeneity: a looking glass for cancer? Nat. Rev. Cancer 12, 323–334. [PubMed: 22513401]

Massagué J (2008). TGFbeta in cancer. Cell 134, 215–230. [PubMed: 18662538]

Minn AJ, Gupta GP, Siegel PM, Bos PD, Shu W, Giri DD, Viale A, Olshen AB, Gerald WL, and Massagué J (2005a). Genes that mediate breast cancer metastasis to lung. Nature 436, 518–524. [PubMed: 16049480]

Minn AJ, Kang Y, Serganova I, Gupta GP, Giri DD, Doubrovin M, Ponomarev V, Gerald WL, Blasberg R, and Massagué J (2005b). Distinct organ-specific metastatic potential of individual breast cancer cells and primary tumors. J. Clin. Invest. 115, 44–55. [PubMed: 15630443]

Neesse A, Michl P, Frese KK, Feig C, Cook N, Jacobetz MA, Lolkema MP, Buchholz M, Olive KP, Gress TM, and Tuveson DA (2011). Stromal biology and therapy in pancreatic cancer. Gut 60, 861–868. [PubMed: 20966025]

Newman MEJ (2003). The structure and function of complex networks. SIAM Review 45, 167–256.

Nguyen DG, Funk J, Robbins JB, Crogan-Grundy C, Presnell SC, Singer T, and Roth AB (2016a). Bioprinted 3D primary liver tissues allow assessment of organ-level response to clinical drug induced toxicity in vitro. PLoS One 11, e0158674. [PubMed: 27387377]

Nguyen DG, King SM, and Presnell SC (2016b). Engineered renal tissues, arrays thereof, and methods of making the same. United States patent, 14/876659.

Nishimura R, Osako T, Okumura Y, Hayashi M, Toyozumi Y, and Arima N (2010). Ki-67 as a prognostic marker according to breast cancer subtype and a predictor of recurrence time in primary breast cancer. Exp. Ther. Med 1, 747–754. [PubMed: 22993598]

Otsu N (1979). Threshold selection method from gray-level histograms. IEEE Trans. Syst. Man Cybern 9, 62–66.

Ozbolat IT, and Hospodiuk M (2016). Current advances and future perspectives in extrusion-based bioprinting. Biomaterials 76, 321–343. [PubMed: 26561931]

Park J, Morley TS, Kim M, Clegg DJ, and Scherer PE (2014). Obesity and cancer–mechanisms underlying tumour progression and recurrence. Nat.Rev. Endocrinol 10, 455–465. [PubMed: 24935119]

Peng W, Unutmaz D, and Ozbolat IT (2016). Bioprinting towards physiologically relevant tissue models for pharmaceutics. Trends Biotechnol. 34, 722–732. [PubMed: 27296078]

Pietras K, and Ostman A (2010). Hallmarks of cancer: interactions with the tumor stroma. Exp. Cell Res. 316, 1324–1331. [PubMed: 20211171]

Plaks V, Kong N, and Werb Z (2015). The cancer stem cell niche: how essential is the niche in regulating stemness of tumor cells? Cell Stem Cell 16, 225–238. [PubMed: 25748930]

Polyak K (2011). Heterogeneity in breast cancer. J. Clin. Invest 121, 3786–3788. [PubMed: 21965334]

Prat A, Parker JS, Karginova O, Fan C, Livasy C, Herschkowitz JI, He X, and Perou CM (2010). Phenotypic and molecular characterization of the claudin-low intrinsic subtype of breast cancer. Breast Cancer Res. 12, R68. [PubMed: 20813035]

Preibisch S, Saalfeld S, and Tomancak P (2009). Globally optimal stitching of tiled 3D microscopic image acquisitions. Bioinformatics 25, 1463–1465. [PubMed: 19346324]

Quail DF, and Joyce JA (2013). Microenvironmental regulation of tumor progression and metastasis. Nat. Med 19, 1423–1437. [PubMed: 24202395]

Schindelin J, Arganda-Carreras I, Frise E, Kaynig V, Longair M, Pietzsch T, Preibisch S, Rueden C, Saalfeld S, Schmid B, et al. (2012). Fiji: an open-source platform for biological-image analysis. Nat. Methods 9, 676–682. [PubMed: 22743772]

Schneider CA, Rasband WS, and Eliceiri KW (2012). NIH Image to ImageJ: 25 years of image analysis. Nat. Methods 9, 671–675. [PubMed: 22930834]

Serra J (1979). [Biomedical image analysis by mathematical morphology (author's transl)]. Pathol. Biol. (Paris) 27, 205–207. [PubMed: 379757]

Sherman MH (2018). Stellate cells in tissue repair, inflammation, and cancer. Annu. Rev. Cell Dev. Biol 34, 333–355. [PubMed: 30028641]

Shi Y, Du L, Lin L, and Wang Y (2017). Tumour-associated mesenchymal stem/stromal cells: emerging therapeutic targets. Nat. Rev. Drug Discov 16, 35–52. [PubMed: 27811929]

Sørlie T, Perou CM, Tibshirani R, Aas T, Geisler S, Johnsen H, Hastie T, Eisen MB, van de Rijn M, Jeffrey SS, et al. (2001). Gene expression patterns of breast carcinomas distinguish tumor

subclasses with clinical implications. Proc. Natl. Acad. Sci. USA 98, 10869–10874. [PubMed: 11553815]

Stadler M, Walter S, Walzl A, Kramer N, Unger C, Scherzer M, Unterleuthner D, Hengstschläger M, Krupitza G, and Dolznig H (2015). Increased complexity in carcinomas: analyzing and modeling the interaction of human cancer cells with their microenvironment. Semin. Cancer Biol 35, 107–124. [PubMed: 26320002]

Vanderburgh J, Sterling JA, and Guelcher SA (2016). 3D Printing of tissue engineered constructs for in vitro modeling of disease progression and drug screening. Ann. Biomed. Eng 45, 164–179. [PubMed: 27169894]

Weigelt B, Ghajar CM, and Bissell MJ (2014). The need for complex 3D culture models to unravel novel pathways and identify accurate biomarkers in breast cancer. Adv. Drug Deliv. Rev 69–70, 42–51.

Xu F, Celli J, Rizvi I, Moon S, Hasan T, and Demirci U (2011). A three-dimensional in vitro ovarian cancer coculture model using a high-throughput cell patterning platform. Biotechnol. J 6, 204–212. [PubMed: 21298805]

Zhang YS, Duchamp M, Oklu R, Ellisen LW, Langer R, and Khademhosseini A (2016b). Bioprinting the Cancer Microenvironment. ACS Biomater Sci. Eng 2, 1710–1721. [PubMed: 28251176]

Zhang YS, Yue K, Aleman J, Mollazadeh-Moghaddam K, Bakht SM, Yang J, Jia W, Dell'Erba V, Assawes P, Shin SR, et al. (2016a). 3D bioprinting for tissue and organ fabrication. Ann. Biomed. Eng 45, 148–163. [PubMed: 27126775]

Zhao Y, Yao R, Ouyang L, Ding H, Zhang T, Zhang K, Cheng S, and Sun W (2014). Three-dimensional printing of Hela cells for cervical tumor model in vitro. Biofabrication 6, 035001. [PubMed: 24722236]

Zhu W, Xu W, Jiang R, Qian H, Chen M, Hu J, Cao W, Han C, and Chen Y (2006). Mesenchymal stem cells derived from bone marrow favor tumor cell growth in vivo. Exp. Mol. Pathol 80, 267–274. [PubMed: 16214129]

Highlights

- Bioprinted tumor tissue is a scaffold-free model of tumor-stromal interactions
- Cells within bioprinted tissues mature, self-organize, and deposit matrix proteins
- Heterogeneity in therapeutic response, migration, and signaling can be assessed
- Primary patient tissue can be bioprinted into tissues for translational studies

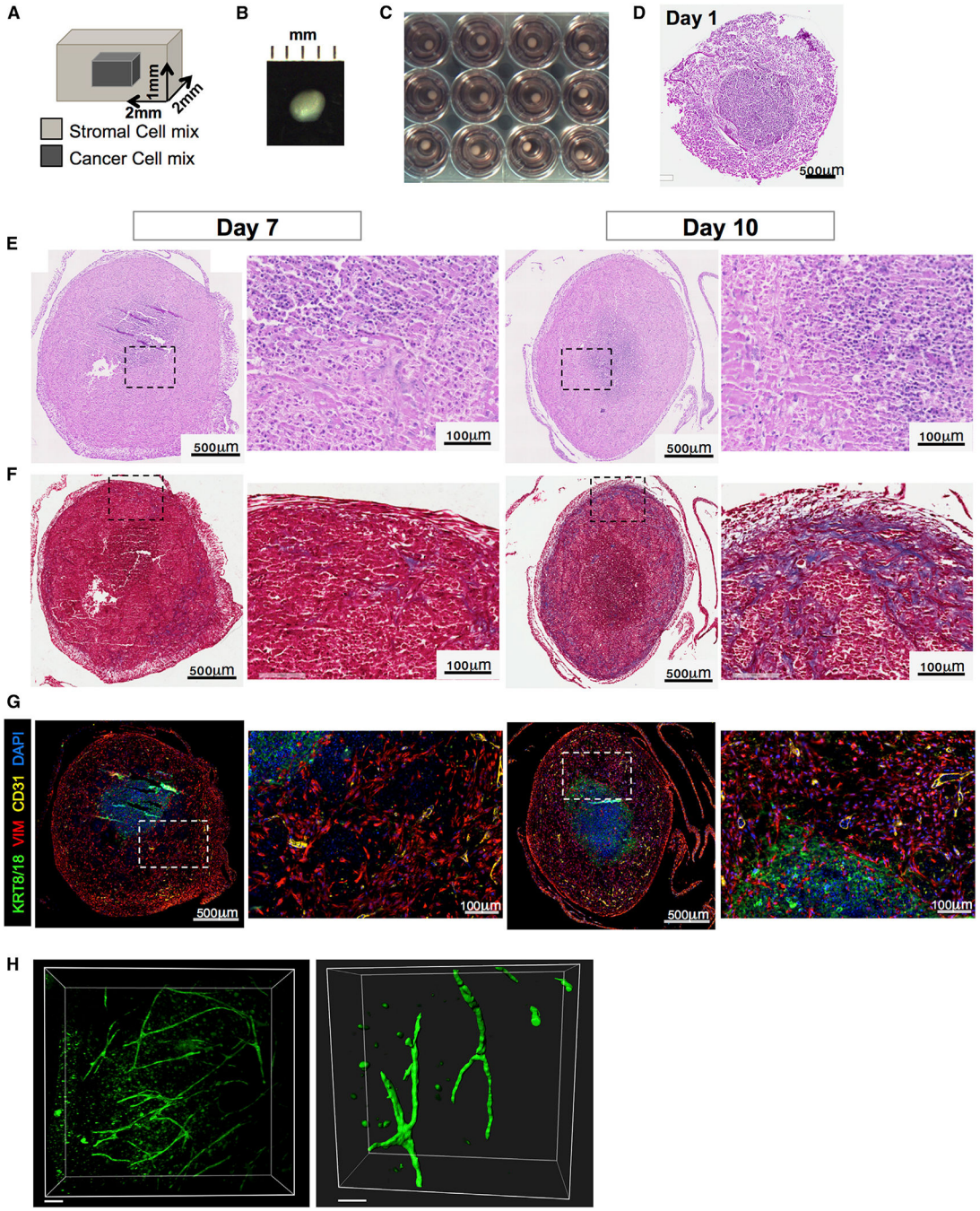

Figure 1. Three-Dimensional Bioprinting Can Generate Models of Tumor Tissues

(A) A schematic of a three-dimensional (3D) bioprinted tissue.

(B) A photograph of a cultured printed tissue depicting the size in millimeters.

(C) Printed tissues cultured on transwells in standard tissue culture plates.

(D) H&E image of a representative printed tumor tissue fixed one day after printing showing the central cancer pocket surrounded by a stromal cell mix.

(E) H&E images of FFPE sections of printed tumor tissues, representative of at least 3 independent experiments. Tissues were printed with MCF-7 cells and HUVECs in the cancer

compartment and HMFs and HUVECs in the stromal compartment. Printed tissues were cultured for 7 or 10 days. Scale bars represent 500 μm or 100 μm as marked.
(F) Masson's trichrome staining of the same bioprinted tissues as in (E). Scale bars represent 500 mm or 100 mm as marked.
(G) Immunofluorescence on sections from bioprinted tissues as above for KRT8/18 (green), vimentin (VIM, red), and CD31 (yellow). DAPI (blue) is a nuclear counterstain. Scale bars represent 500 μm or 100 μm as marked.
(H) Left: 3D Digital reconstruction of immunofluorescence on CLARITY-processed bioprinted tissue stained for CD31 (green). Right: Digital surface coating showing detailed architecture of endothelial networks. Similar results were seen in two bioprinted tissues. Scale bars represent 100 μm (left) and 50 μm (right).
Full scans were digitally stitched by the appropriate image software as described in STAR Methods. See also Figure S1.

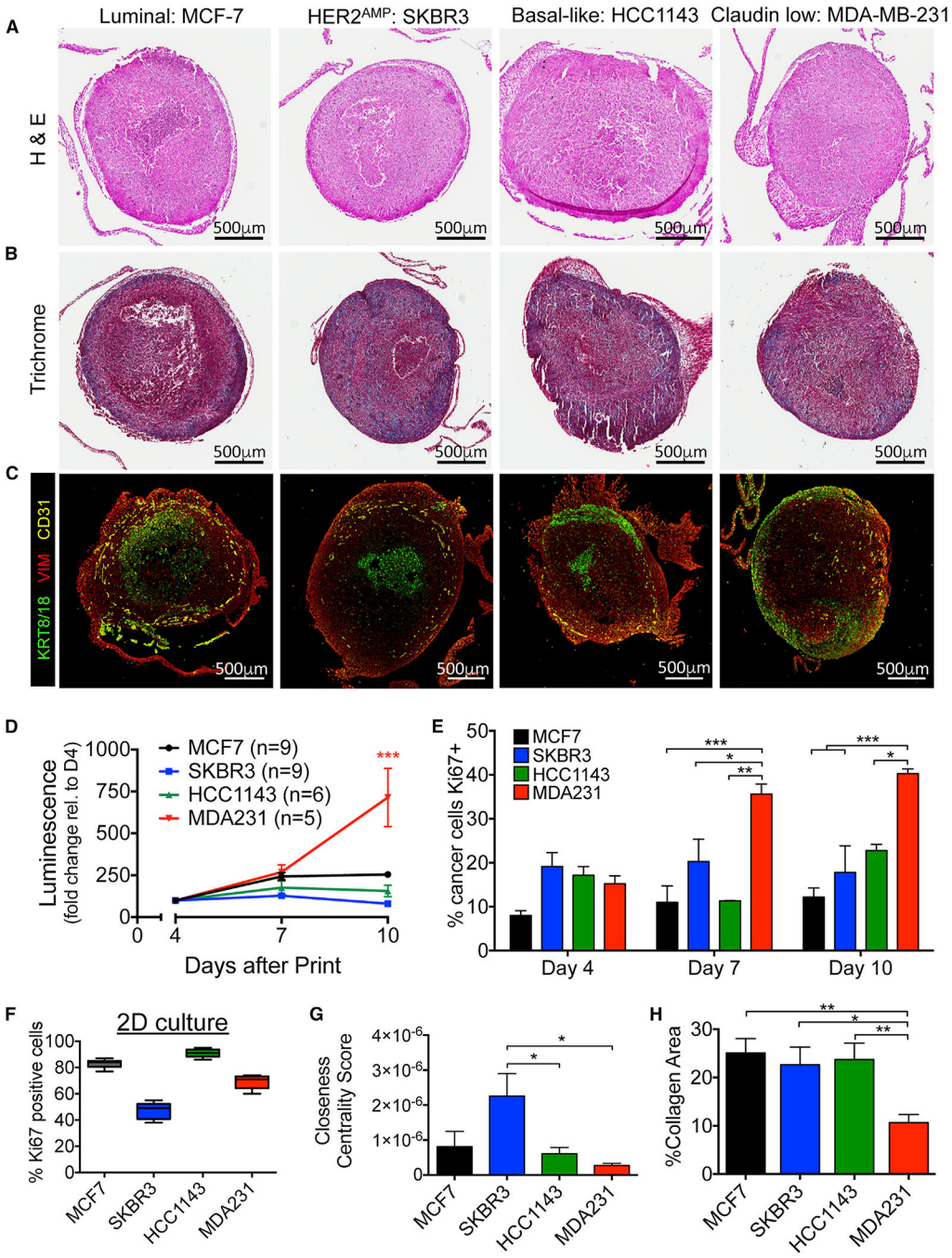

Figure 2. Bioprinted Tissues Can Model Distinct Tumor Cell Subtypes

(A) Representative H&E images of tissues bioprinted with luminal (MCF-7), HER2^{AMP} (SKBR3), basal-like (HCC1143), or claudin-low (MDA-MB-231) breast cancer cell lines. All tissues were printed into a stromal mix of HMFs and HUVECs and fixed on day 10. Scale bars represent 500 μm. Representative of 3 independent experiments.

(B) Trichrome staining of tissues as described in (A). Scale bars represent 500 μm.

(C) Immunofluorescence on sections from bioprinted tissues, as described in (A), stained for KRT8/18 (green), VIM (red), and CD31 (yellow). Scale bars represent500 μm.

(D) Luciferase quantitation of relative cancer cell number in bioprinted tissues, as described in (A), over time. Shown is the average ± SEM of at least 5 structures for each cell type representing two independent experiments. MDA-MB-231 endpoint luminescence is significantly different than the other 3 cell lines. ***$p < 0.001$ from one-way ANOVA.
(E) Quantitation of Ki67-positive cancer and stromal cells as assessed from immunofluorescence (IF) images. Shown is average ± SEM of at least 3 tissues at each time point, except for HCC1143 at day 7 (2 tissues). Representative images are shown in Figure S2A. ***$p < 0.001$; **$p < 0.01$; and *$p < 0.05$ by two-way ANOVA.
(F) Quantification of Ki67-positive cells in MCF-7, SKBR3, HCC1143, or MDA-MB-231 cells grown in standard 2D culture. Tukey boxplot of two individual experiments with 6 technical replicates per experiment.
(G) Quantitation of the cancer cell closeness centrality score in at least 7 tissues for each cell line over two independent experiments. Shown is the average ± SEM. Representative images and masking is shown in Figure S3A. *$p < 0.05$ by a one-way ANOVA.
(H) Quantitation of trichrome staining in bioprinted tissues from (A). Shown is average ± SEM of at least 6 tissues over two independent experiments. *$p < 0.05$ and **$p < 0.01$ by a two-tailed t test.
Full scans were digitally stitched by the appropriate image software as described in STAR Methods. See also Figures S1, S2, and S3.

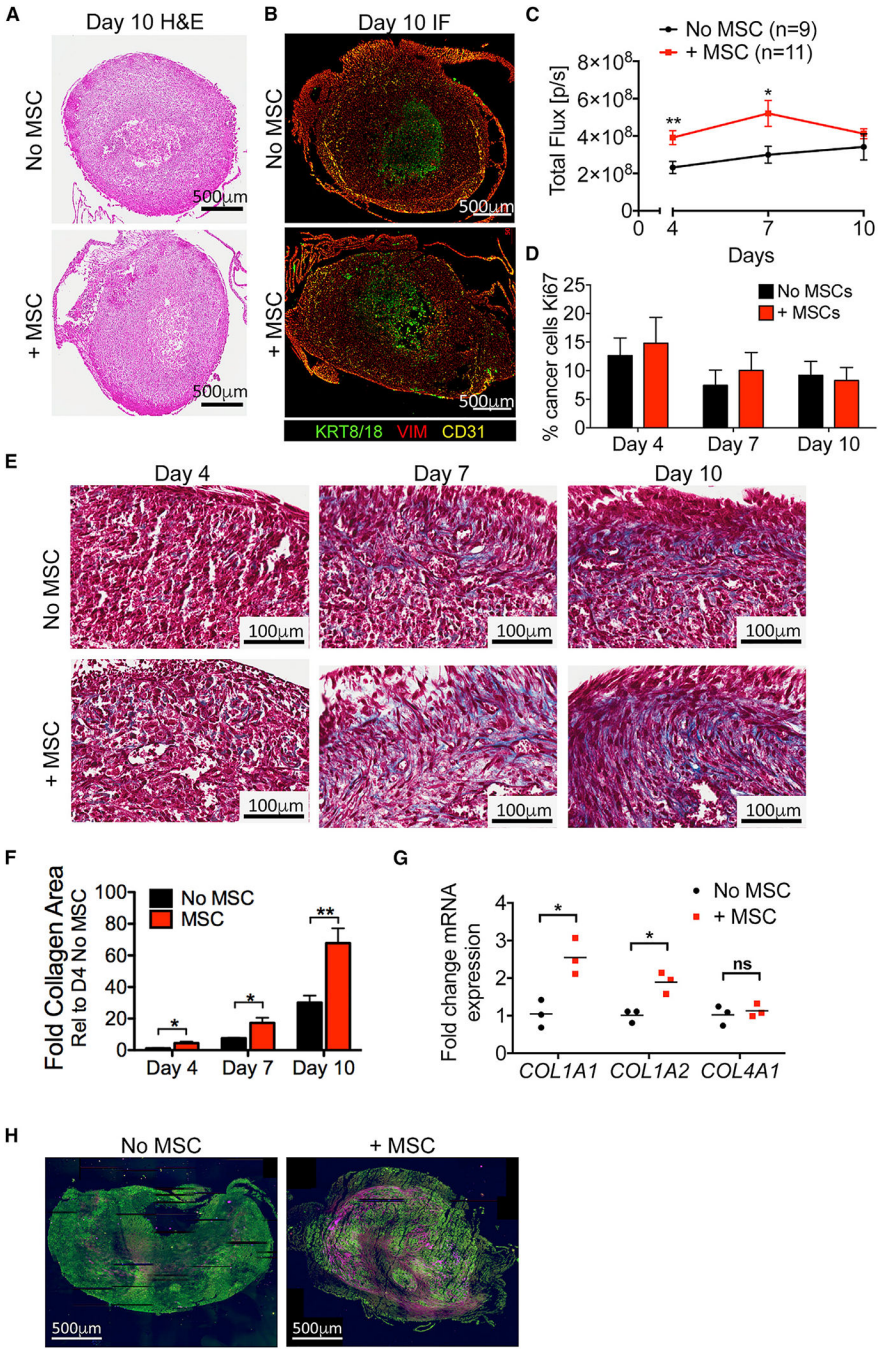

Figure 3. Distinct Microenvironments Can Be Modeled in Bioprinted Tissues

(A) Representative H&E staining of day 10 MCF-7 breast cancer tissues without (top panel) or with (bottom panel) MSCs in the stromal compartment at a ratio of50% HMFs, 25% HUVECs, and 25% MSCs.

(B) Representative IF images of day 10 MCF-7 breast cancer tissues as in panel A stained for KRT8/18 (green), VIM (red), and CD31 (yellow).

(C) Average luciferase readings over time in MCF-7 tissues printed as in (A) ± SEM. *$p < 0.05$ and **$p < 0.01$ by a two-tailed t test.

(D) Quantitation of the percentage of Ki67-positive cells in MCF-7 tissues printed as in (A). Shown is the average ± SEM of at least 8 tissues representing two independent experiments that were analyzed at each time point.
(E) Representative Masson's trichrome staining of bioprinted tissues as in (A), fixed on day 4, 7, or 10. Scale bars represent 100 μm.
(F) ImageJ quantitation of trichrome staining on tissues from (E). Shown is the average ± SEM of at least six bioprinted tissues per time point in each condition across two independent experiments. *$p < 0.05$ and **$p < 0.01$ by a two-tailed t test.
(G) qRT-PCR for collagen genes in tissues printed as in (A) (n = 3 tissues), relative to the average "no MSC" value. *$p < 0.05$ by a two-tailed t test. ns denotes not significant.
(H) Digitally stitched second harmonic generation (SHG) images of day 7 bioprinted tissues in a separate MCF-7 print with and without MSCs. Purple color represents signal of mature collagen. n = two tissues per condition.
Full scans were digitally stitched by the appropriate image software as described in STAR Methods. See also Figure S4.

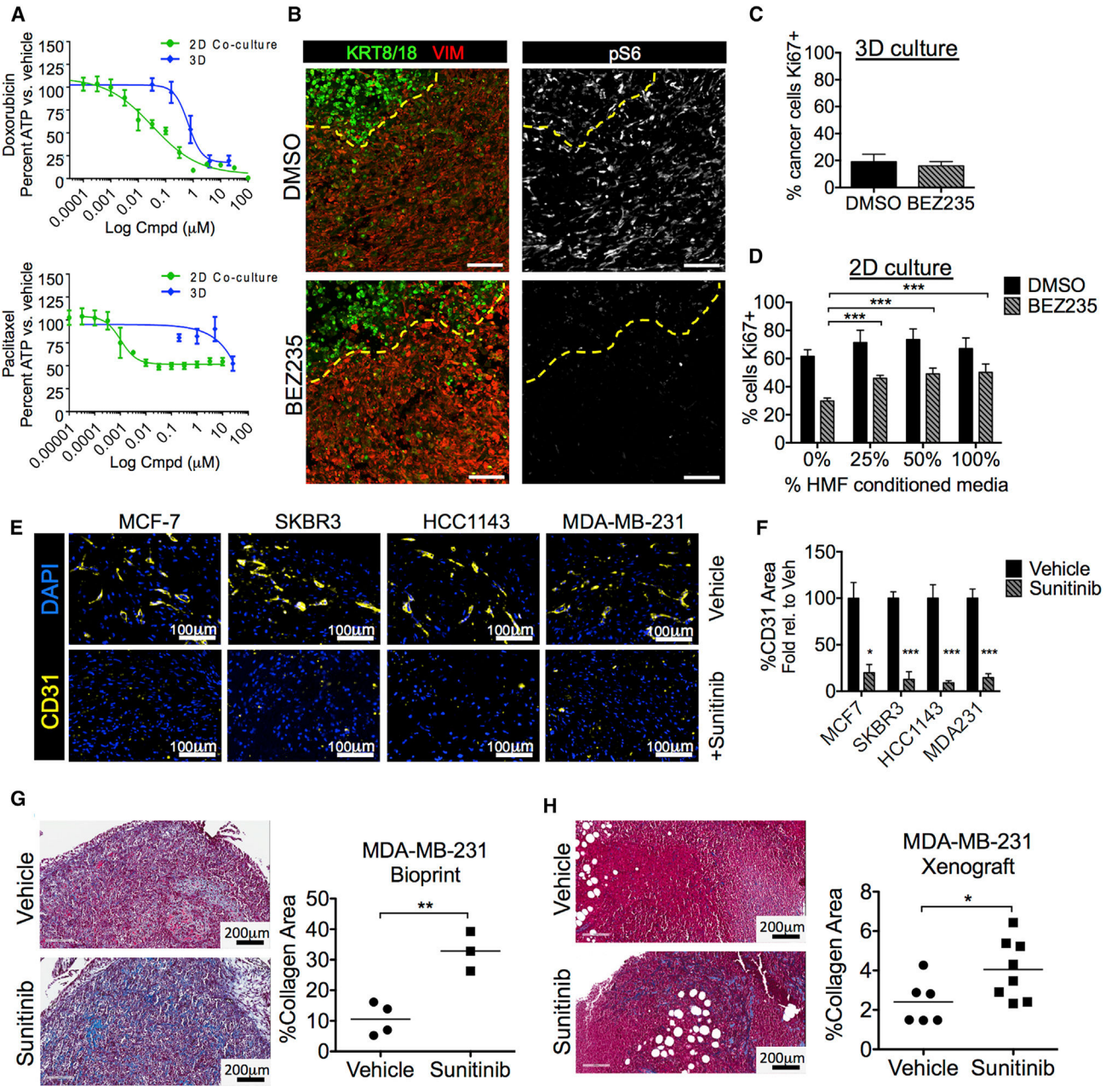

Figure 4. Bioprinted Tissues Can Be Utilized to Assess Therapeutic Efficacy

(A) Dose response curves for 3D bioprinted MCF-7 breast cancer tissues containing preadipocytes (bioprinted as in Figure S4A), compared to 2D co-cultures with the same ratio of cell types. Tissues or cells were treated with doxorubicin or paclitaxel and assessed by ATP utilization assay. Average of 9 replicates ± SEM shown.

(B) Representative IF images of HCC1143 bioprinted tissues treated with DMSO or BEZ235. Cells were stained for VIM (red), KRT8/18 (green), and pS6 (shown in white in right panels). Scale bars represent 100 μm.

(C) Quantitation of Ki67-positive cancer cells in HCC1143 bioprinted tissues from (B), treated with vehicle or BEZ235; shown is the average ± SEM of 4 structures per condition.

(D) Quantitation of Ki67-positive HCC1143 cells grown in 2D culture and treated with vehicle or BEZ235 in the presence of the indicated percent of HMF-conditioned medium. Shown is the average of 3 independent experiments with 3 replicates each ± SD and ***$p < 0.001$ by a two-way ANOVA.

(E) IF on tissues bioprinted with MCF-7, SKBR3, HCC1143, or MDA-MB-231 breast cancer cell lines for CD31 (yellow). DAPI (blue) is a nuclear counterstain. Bioprinted tissues were left untreated (top row) or treated beginning on day 4 with 1 μM Sunitinib (bottom row). Scale bars represent 100 μm.

(F) Quantitation of CD31 staining on tissues printed and treated as in (D). Average ± SEM of 4–12 tissues per cell line were quantified across at least two independent experiments. *$p < 0.05$; and ***$p < 0.001$ by a two-tailed t test.

(G) Representative images (left) and quantitation (right) of trichrome staining in MDA-MB-231 bioprinted tissues treated with or without Sunitinib. Shown is average of 4 vehicle and 3 Sunitinib bioprinted tissues. **$p < 0.01$ by a two-tailed t test.

(H) Representative images (left) and quantitation (right) of trichrome staining in MDA-MB-231 xenografts treated with or without Sunitinib. Shown is average of 7 vehicle and 8 Sunitinib tumors, 3–6 images per tumor. *$p < 0.05$ by a two-tailed t test.

Full scans were digitally stitched by the appropriate image software as described in STAR Methods. See also Figure S5.

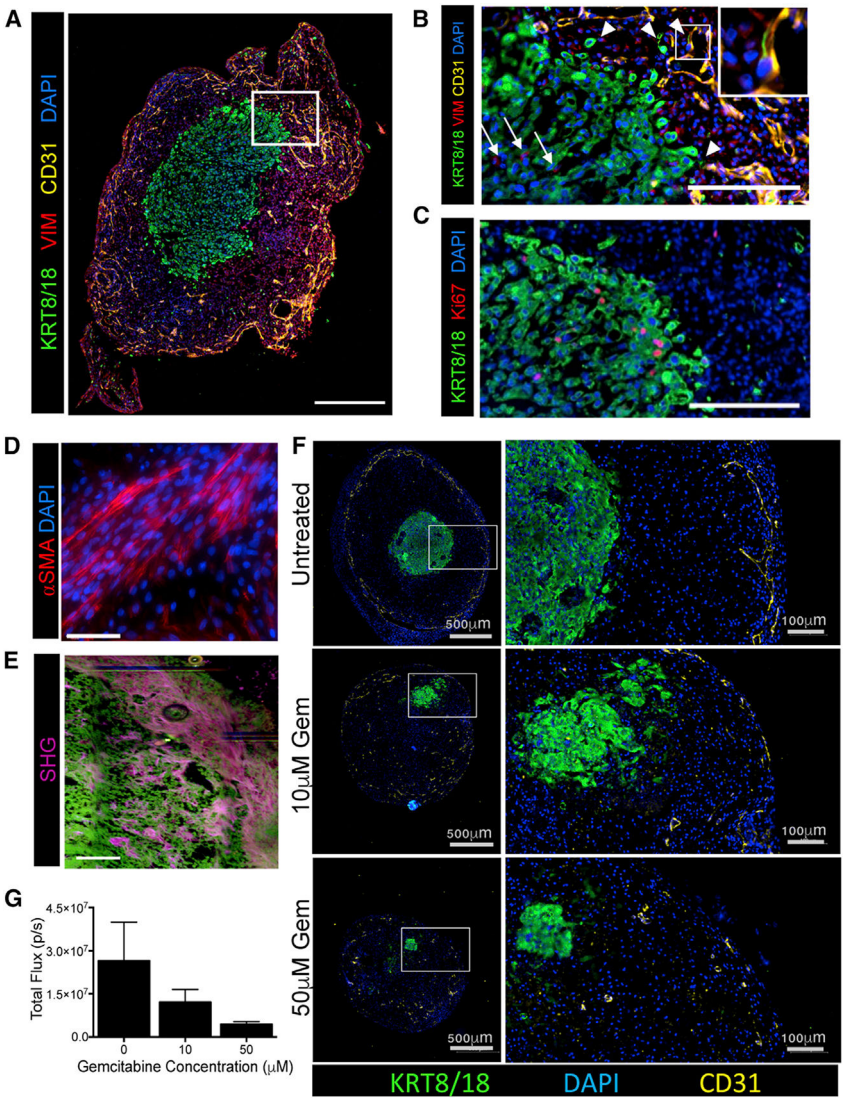

Figure 5. Three-Dimensional Bioprinting Can Model Additional Tumor Types, Including Pancreatic Cancer

(A) Bioprinted tissue containing a patient-derived xenograft (PDX)-derived cell line from OPTR3099C surrounded by PSCs and HUVECs after 7 days in culture. Tissues were placed immediately into complete medium without crosslinking. IF for KRT8/18 (green), VIM (red), and CD31 (yellow) with DAPI (blue) nuclear counterstain. Scale bar represents 500 μm. White box denotes inset shown in Figure 5B

(B) Inset of Figure 5A showing the tumor-stromal border. Arrows indicate VIM-positive cells within the tumor core, and arrowheads show KRT8/18 cells in the stroma. Inset of white box shows interaction between cancer and endothelial cells. Scale bar represents 200 μm.

(C) IF on a serial section to panel B for KRT8/18 (green) and Ki67 (red) with DAPI (blue) nuclear counterstain. Scale bar represents 200 μm.

(D) IF for α-SMA in PSCs after 7 days in culture. Structures were printed as in (A), with the exception of 12.5% HUVECs. Scale bar represents 50 μm.

(E) Digitally stitched SHG image on bioprinted pancreatic tumor tissue printed with PSCs and HUVECs in the stromal compartment and HPAFIIs and HUVECs in the cancer compartment. Imaging was done on tissues cultured for 10 days. Scale bar represents 100 μm.

(F) Pancreatic tumor tissues printed as in (E) were treated for 6 days with either 10 or 50 μM gemcitabine. Bioprinted tissues were fixed on day 10 (6 days of treatment) and IF performed for KRT8/18 (green) and CD31 (yellow) with DAPI (blue) nuclear counterstain. White box indicates region of inset shown on right. Scale bars represent 500 μm or 100 μm as indicated.

(G) Day 10 IVIS quantitation of total flux for bioprinted tissues grown as in (E). Shown is the average of 6 individual tissues across two individual experiments ± SEM.

Full scans were digitally stitched by the appropriate image software as described in STAR Methods. See also Figure S6.

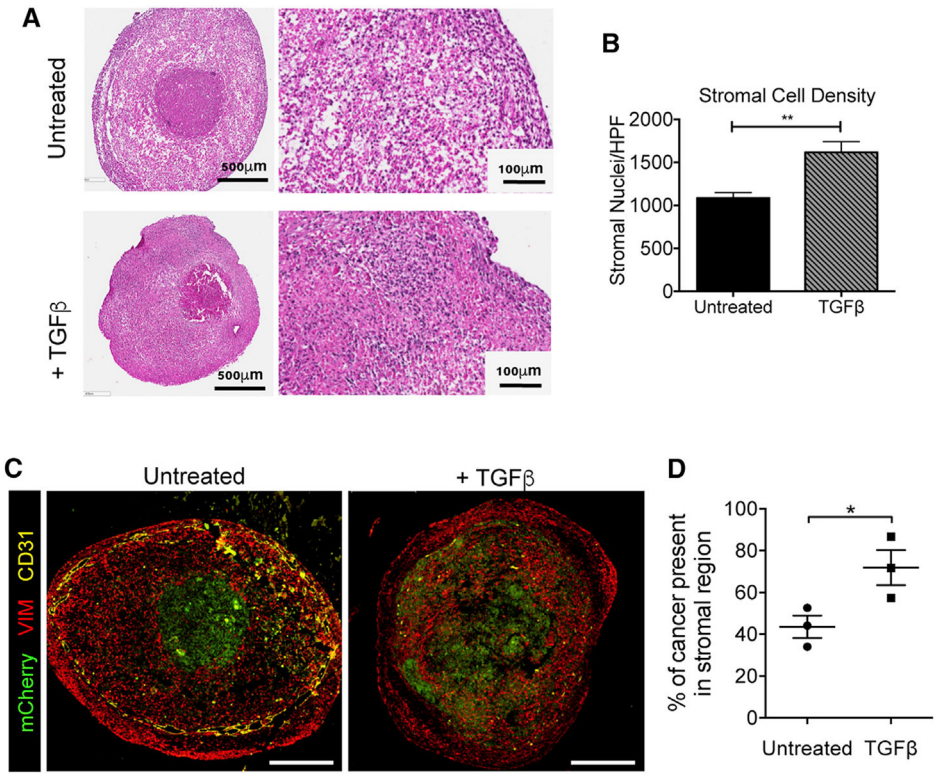

Figure 6. Cancer and Stromal Cells Respond to Microenvironmental Signals in Bioprinted Tumors

(A) H&E staining of pancreatic tumor tissues printed with PSCs and HUVECs in the stromal compartment and HPAFIIs and HUVECs in the cancer compartment. Bioprinted tissues were treated daily with 5 ng/mL TGFβ starting 24 h after printing, and all tissues were fixed on day 10. Scale bar represents 500 μm and 100 μm.

(B) Average cellular density of the stromal compartment was quantified in ImageJ from 3 203 images each from at least 3 bioprinted tissues in each condition. Error bars represent ± SD. **$p < 0.01$ by a two tailed t test.

(C) Fluorescent images of bioprinted tissues as in (A) for mCherry (green), VIM (red), and CD31 (yellow). Scale bars represent 500 μm.

(D) Quantification of the percent of mCherry-positive cancer within the stromal region in untreated and TGFβ treated tissues. Shown is the average ± SEM of 3 structures per condition. *$p < 0.05$ by a two-tailed t test.

Full scans were digitally stitched by the appropriate image software as described in STAR Methods.

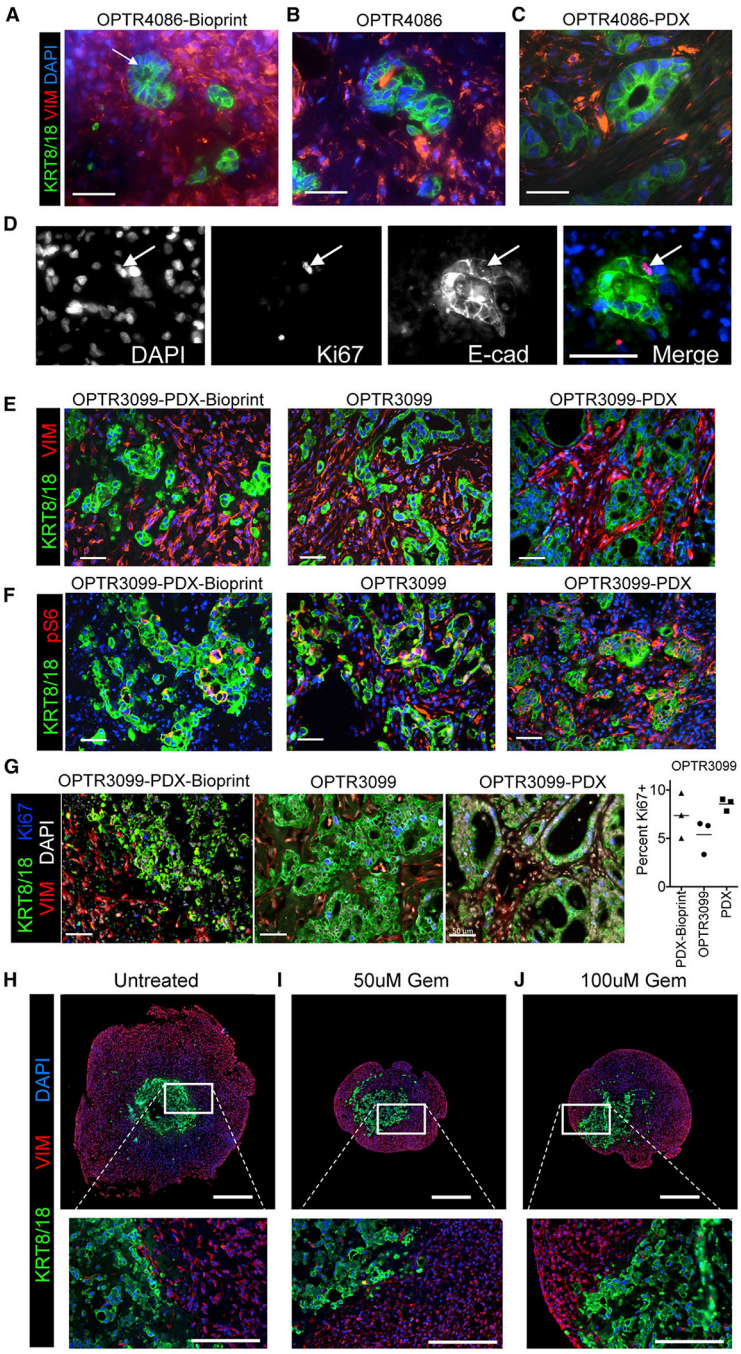

Figure 7. Bioprinted Tissues Generated from Primary Patient Tumors Recapitulate *In Vivo* Morphology

(A–C) IF for KRT8/18 (green) and VIM (red) with DAPI (blue) nuclear stain on bioprinted tissue with PSCs and HUVECs in the stromal compartment and disassociated primary patient tumor tissue from OPTR4086 in the cancer compartment (OPTR4086-Bioprint) (A), primary patient tissue from OPTR4086 (B), and PDX tumor tissue generated from OPTR4086 (C). Arrow indicates luminal space. Scale bars for panels (A)–(F) represent 50 μm.

(D) IF for E-cadherin (E-cad) (green) and Ki67 (red) with DAPI (blue) nuclear stain.

(E and F) IF for KRT8/18 (green) and VIM (red) (E) or KRT8/18 (green) and pS6 (red) (F) with DAPI (blue) nuclear stain in OPTR3099-PDX-Bioprint tissue (PSCs and HUVECs in the stromal compartment with disassociated PDX tumor tissue generated from OPTR3099 in the cancer compartment), primary patient tissue from OPTR3099, and PDX tumor tissue generated from OPTR3099 (OPTR3099-PDX).

(G) IF for KRT8/18 (green), VIM (red), and Ki67 (blue) with DAPI (gray) nuclear stain from tissues printed as in (E). Quantification of the percentage of Ki67+/KRT8/18+ dual positive cells shown on right. Average of 3 independent structures shown for OPTR3099-PDX-Bioprint and 3 randomly selected 10× fields for OPTR3099 and OPTR3099-PDX tumor tissue.

(H–J) Bioprinted tissue generated as in (E) and treated for 3 days with vehicle (H) or 50 μM (I) or 100 μM (J) of gemcitabine starting at day 4 in culture. IF for KRT8/18 (green) and VIM (red) with DAPI (blue) nuclear stain on bioprinted tissues at day 7 (3 days of treatment). Scale bars represent 500 μm. White box denotes insets of panels (H)–(J) shown below. n = 2–3 structures per condition. Scale bars represent 200 μm.

Full scans were digitally stitched by the appropriate image software as described in STAR Methods. See also Figure S7.

KEY RESOURCES TABLE

REAGENT or RESOURCE	SOURCE	IDENTIFIED
Antibodies		
Guinea Pig polyclonal anti-KRT8/18	Fitzgerald	Cat #: 20R-CP004
		RRID: AB_1284055
Rabbit monoclonal anti-VIM [D21H3]	Cell Signaling	Cat #: 5741S
		RRID: AB_10695459
Rat monoclonal anti-VIM [280618]	R&D Systems	Cat #: MAB2105
		RRID: AB_2241653
Mouse monoclonal anti-CD31 [89C2]	Cell Signaling	Cat #: 3528S
		RRID: AB_2160882
Rabbit polyclonal anti-alpha smooth muscle Actin	Abcam	Cat #: ab5694
		RRID: AB_2223021
Rabbit polyclonal anti-Ki67	Leica	Cat #: NCL-Ki67p
		RRID: AB_442102
Rabbit monoclonal anti-Ki67 [D3B5]	Cell Signaling	Cat #: 12202S
		RRID: AB_2620142
Rat monoclonal anti-Ki67 eFluor570 [SolA15]	Thermo Fisher	Cat #: 41–5698-80
		RRID: AB_11219874
Mouse monoclonal anti-E-cadherin [36/E-cadherin]	BD Biosciences	Cat #: 610181
		RRID: AB_397580
Rabbit monoclonal anti-Phospho-S6 Ribosomal Protein (Ser240/244) [D68F8]	Cell Signaling	Cat #: 5364S
		RRID: AB_10694233
Rabbit monoclonal anti-Ku80 [C48E7]	Cell Signaling	Cat #: 2180S
		RRID: AB_2218736
Biological Samples		
Primary patient tissue OPTR4086 (female)	This paper	N/A
Primary patient tissue OPTR3099 (male)	This paper	N/A
PDX	This paper	OPTR3099-PDX
Chemicals, Peptides, and Recombinant Proteins		
Sunitinib, Malate Salt	LC Laboratories	Cat #: S-8803
		CAS: 341031–54-7
Gelatin	MilliporeSigma	Cat #: G2500
		CAS: 9000–70-8
Pronova UP LVG Sodium Alginate	NovaMatrix	Cat #: 4200006
Alginate Lyase	MilliporeSigma	Cat #: A1603
		CAS: 9024–15-1
Xenolight D-Luciferin – K+salt Bioluminescent Substrate	Perkin Elmer	Cat #: 122799
Recombinant Human TGF-beta	Peprotech	Cat #: 100–21
Doxorubicin	CAS: 23214–92-8	

REAGENT or RESOURCE	SOURCE	IDENTIFIED
Paclitaxel	CAS: 33069–62-4	
BEZ235	SelleckChem	Cat #: S1009
		CAS: 915019–65-7
Gemcitabine, Hydrochloride salt	LC Laboratories	Cat #: G4177
		CAS: 122111–03-9
Critical Commercial Assays		
Human Leptin ELISA Kit	Thermo Fisher	Cat #: KAC2281
Cell Titer Glo assay	Promega	Cat #: G7571
Experimental Models: Cell Lines		
Human Mammary Fibroblasts	ScienCell	Cat #: 7630
		Multiple lots used (all female)
Human Umbilical Vein Endothelial Cells	BD Biosciences	Cat #: 354151
		Lot: 19461 (female)
Human Umbilical Vein Endothelial Cells	MilliporeSigma	Cat #: SCCE001
		Multiple lots used (sex unknown)
Human Pulmonary Microvascular Endothelial Cells	ScienCell	Cat #: 3000
		Lot: 3478 (sex unknown)
Human Adult Pulmonary Fibroblasts	ScienCell	Cat #: 3310
		Lot: 1439 (female)
Human Subcutaneous Preadipocytes	Zen-Bio	Cat #: SP-F-SL
		Mixed donors
Human Pancreatic Stellate Cells	ScienCell	Cat #: 3830
		Lots: 10473 and 10295 (both male)
Human Bone Marrow Derived Mesenchymal Stem Cells	ScienCell	Cat #: 7500
		Lots: 21580 (female) and 6881 (sex unknown)
HPAFII	ATCC	Cat #: CRL-1997
		Sex: male
MDA-MB-231	ATCC	Cat #: HTB-26
		Sex: female
SKBR3	ATCC	Cat #: HTB-30
		Sex: female
A549	ATCC	Cat #: CCL-185
		Sex: male
HCC1143	ATCC	Cat #: CRL-2321
		Sex: female
MCF7	MilliporeSigma	Cat #: 86012803–1VL
		Sex: female
MCF7	ATCC	Cat #: HTB-22
		Sex: female

REAGENT or RESOURCE	SOURCE	IDENTIFIED
OPTR3099 primary cell line	This paper	Sex: male
Experimental Models: Organisms/Strains		
NOD.Cg-*Prkdcscid Il2rgtm1Wjl*/SzJ	Jackson labs	RRID: IMSR_JAX:005557
Oligonucleotides		
COL1A1 For:	IDT, sequence from Corsa et al., 2016	N/A
GAGGGCCAAGACGAAGACATC		
COL1A1 Rev:	IDT, sequence from Corsa et al., 2016	N/A
CAGATCACGTCATCGCACAAC		
COL1A2 For:	IDT, sequence from Corsa et al., 2016	N/A
GGCCCTCAAGGTTTCCAAGG		
COL1A2 Rev:	IDT, sequence from Corsa et al., 2016	N/A
CACCCTGTGGTCCAACAACTC		
COL4A1 For:	IDT, sequence from Corsa et al., 2016	N/A
ATGGGGCCCCGGCTCAGC		
COL4A1 Rev:	IDT, sequence from Corsa et al., 2016	N/A
ATCCTCTTTCACCTTTCAATAGC		
TBP For:	IDT, sequence from Bié che et al., 2003	N/A
TGCACAGGAGCCAAGAGTGAA		
TBP Rev:	IDT, sequence from Bié che et al., 2003	N/A
CACATCACAGCTCCCCACCA		
Recombinant DNA		
pLV416G vector	Collisson et al., 2011	N/A
Software and Algorithms		
ImageJ	Opensource	Version 1.51
		https://imagej.nih.gov/ij/
FIJI	Opensource	https://fiji.sc/
CellProfiler	Opensource	Version 2.1.1
		https://cellprofiler.org/
Zen	Zeiss Microscopy	Version 2.3
Prism	GraphPad	Versions 5 and 6
Imaris software	Bitplane	Version 10
Software and scripts for marker expression in 3D tissues (Figures 2E, 2G, 3D, 4C, S2B, S2C, S4D, S4E, and S7C)	This paper	Supplemental Data S1
Cell profiler script for Ki67 quantitation in 2D culture (Figures 2F and 4D)	This paper	Table S1
Algorithm for calling cancer versus stromal cell types and determining CCS for 3D tissues (Figures 2G, S4E, and S7C)	This paper	Supplemental Data S2. Libraries available at: https://github.com/ivanbrugere/matlabnetworks-toolbox.
ImageJ script for Trichrome quantitation (Figures 2H, 3F, 4G, and 4H)	This paper	Table S2